A comparative study on the dynamic performance of floating and submerged wave energy converter arrays

Kai Zhu[a,b], Deborah Greaves[b], Hongda Shi[a,c,d,*], Zhiwen Wei[a], Tianyuan Wang[a], Qing Lu[a], Xiaojie Shi[a,*], Meng Han[a,b], Feifei Cao[a,c]

[a]*Department of Ocean Engineering, College of Engineering, Ocean University of China, Qingdao 266100, China*
[b]*School of Engineering, Computing and Mathematics, University of Plymouth, Drake Circus, Plymouth PL4 8AA, UK*
[c]*Shandong Provincial Key Laboratory of Ocean Engineering, Ocean University of China, Qingdao 266100, China*
[d]*Qingdao Municipal Key Laboratory of Ocean Renewable Energy, Ocean University of China, Qingdao 266100, China*

Abstract

A mathematical model has been formulated to evaluate the dynamic performance of floating buoy (FB) and full-submerged (CETO) wave energy converters (WECs) array. In the process, the boundary value problem is solved by applying the matching-method of eigenfunctions and multi-body Graf's addition to solve the velocity potential that can be decomposed into radiation and diffraction problems. To evaluate the motion and wave energy capture response of WECs, coupled equations of motion are considered, including the PTO damping system, stiffness system, and mooring lines. After running the convergence analysis and model validation, the present model is employed to perform a multimode impact analysis of FB and CETO systems. Case studies clearly reveal the effects of PTO damping, stiffness, geometric dimensions, and submergence depth on the wave energy capture efficiency, bandwidth, and peak frequency in the CETO system. More importantly, comparative analysis of array-based floating and submerged WECs reveals significant performance disparities relative to standalone configurations. Specifically, the standalone FB system demonstrates superior wave energy capture compared to the CETO system, whereas the performance of array-based systems remains inconsistent. This divergence in CETO array performance stems from attenuated shadow effect, balanced energy distribution across array subunits, superior motion stability, and moderated wave elevations, alongside optimized hydrodynamic interactions between units. Consequently, this study constitutes a pioneering demonstration that future CETO system investigations should focus on array-based configurations, which attain wave energy harvesting efficiencies commensurate with FB systems while exhibiting superior motion stability, thereby offering promising prospects for the development of the CETO system.

Keywords: Wave energy converter, Wave-structure interaction, Array-based, Wave energy capture, Motion response

1. Introduction

Ocean waves possess immense potential as a renewable energy resource, yet the exploitation of wave energy has yet to coalesce around a dominant design archetype, with no commercialized projects presently operational [1]. Principal impediments to progress include the limited operational reliability of wave energy converters (WECs) and prohibitively high levelized costs of energy (LCoE). These challenges do not contradict the fundamental principles of WEC technology. Conventionally, WECs employ multistage energy conversion processes, wherein wave energy is first transformed into mechanical energy via a power take-off (PTO) mechanism, subsequently converted to electrical output [2]. Crucially, the kinematic response during mechanical energy conversion is governed by wave amplitude and periodicity, inducing complex wave-structure interactions. While many marine engineering systems prioritize mitigating hydrodynamic forces from such interactions to preserve structural safety [3], WECs conversely seek to optimize

*Corresponding author
Email address: kai.zhu@plymouth.ac.uk (K. Zhu); deborah.greaves@plymouth.ac.uk(D. Greaves); hongda.shi@ouc.edu.cn (H. Shi); shixiaojie@ouc.edu.cn (X. Shi); caofeifei@ouc.edu.cn (F. Cao).

these dynamics for maximal energy harvesting and mechanical output amplification. This operational paradigm, however, exacerbates susceptibility to structural fatigue, substantially elevating operation and maintenance (O&M) costs [4]. Within this framework, numerous technological innovations in WEC design have emerged, prioritizing both enhanced operational stability and robust torque generation capabilities. Among these advancements is the CETO system developed by Carnegie Clean Energy [5], a pioneering solution exemplifying these dual objectives, as illustrated in Fig. 1.

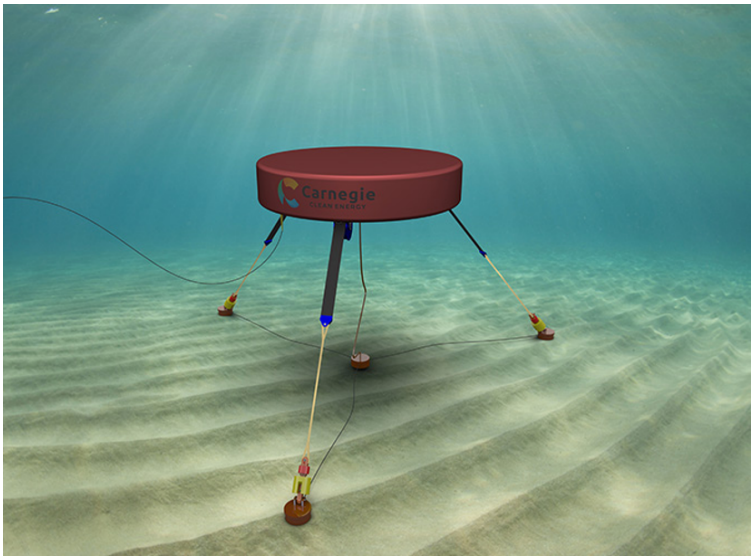

Fig. 1. Three-tethered CETO-6 wave energy converter [5].

In the commercialization process, given the correlation between the wavelength and the characteristic length of the devices, it is crucial for all WECs, irrespective of the type, to be arranged in arrays or wave farms to facilitate electricity generation on a commercial scale [6]. Under array-based configurations, several potential impacts may arise: (a) The shadow effect, caused by the partial blockage of the incident wave field by front-row devices, leads to uneven energy distribution within the array [7]. Devices in the front rows or specific regions may receive higher energy flux, whereas downstream units experience reduced excitation and power absorption, resulting in partial energy loss across the array. The total reduction in capture power can reach up to approximately 25% under specific array spacings and wave parameters [8]. (b) The trapped-wave phenomenon, generated by the interaction between diffraction and radiation waves among multiple floats [9, 10], can induce constructive interference under certain array spacings or resonant conditions (e.g., Bragg resonance) [11]. This may cause local amplification of wave elevation and hydrodynamic pressure, potentially imposing excessive loads on specific devices. (c) Given the limitations of bathymetric conditions in commercial construction, most wave farms are typically located nearshore, where the disturbance of wave fields by large arrays may alter the natural conditions of the littoral zone, leading to erosion or accretion of adjacent beaches and negatively impacting recreational activities in the surrounding areas [1].

Consequently, pursuing enhanced operational stability while mitigating detrimental wave-structure interactions, array-based submerged WEC systems (denoted as CETO) may present distinct advantages over floating-buoy configurations (denoted as FB), as demonstrated below:

(i) Substantially improved motion stability, mitigating wave-induced structural fatigue and prolonging device longevity.

(ii) Significantly attenuated shadow effect, preserving capture efficiency across scaled arrays while preventing concentrated hydrodynamic stresses on individual units.

(iii) Gentler wave surface, minimizing perturbations to nearshore hydrodynamic regimes and associated coastal ecosystem disturbances.

(iv) Considerable energy capture capability, maintaining a competitive energy absorption capacity compared to FB systems in practical implementation scenarios.

Furthermore, current research on CETO remains relatively underdeveloped compared with the more extensively documented studies on FB systems. Of these, Tran et al. [12] investigated critical design parameters of triple-tethered CETO systems, demonstrating that strategic modulation of tether configurations enables hydrodynamic control over surge, heave, and pitch motions, thereby optimizing energy harvesting. Rijnsdorp et al. [1] developed a novel numerical methodology within the hydrostatic framework, implemented through the open-source SWASH model, to simulate wave evolution and wave-WEC interactions across realistic coastal bathymetries. This approach facilitates large-scale assessment of submerged converter hydrodynamic performance in nearshore environments. Jahangir and Ghanbari Motlagh [13] conducted a socioeconomic assessment of CETO deployment for coastal electrification, analyzing a 300-household case study across the Caspian Sea, Persian Gulf, and Oman Sea littorals. Their techno-economic evaluation revealed LCOE ranging from 0.523 to 0.991 $/kWh at the Konarak site, contingent upon WEC deployment density and spatial configuration. David et al. [6] established a multi-objective optimization framework enabling the evaluation of competing performance trade-offs for submerged CETO arrays. Their methodological advancement addressed hydrodynamic interactions in array configurations spanning 5 to 20 units, employing device specifications analogous to Carnegie Clean Energy's CETO-6 technology. Notwithstanding these advancements, the study's scope excluded comparative hydrodynamic performance assessments against FB array systems at equivalent deployment scales. Most relevant to the present study, Sergiienko et al. [14] compared the energy capture efficiency and motion response characteristics of standalone FB and CETO systems, concluding that the FB system significantly outperforms the CETO system in terms of energy capture across nearly all sea states. However, their investigation was confined to individual device configurations, failing to address array-interaction dynamics or assess wave farm performance at scale. This critical knowledge gap underscores the novelty of our study, which pioneers the first comparison of hydrodynamic responses in array-configured FB and CETO systems. Through integrated analysis of energy capture performance and motion stability metrics, we evaluate the technical viability of submerged CETO arrays as a resilient alternative for large-scale wave energy conversion, thereby advancing both fundamental understanding and practical implementation frameworks for marine renewable energy systems.

Contemporary investigation methodologies for array-configured WECs are categorized into three principal methodological domains: physical modeling, numerical simulation, and mathematical modeling. The experimental work by Stratigaki et al. [15, 16] pioneered a 5×5 WEC array configuration (N=25 units), representing one of the most extensive physical array investigations conducted to date [17]. This scale limitation primarily stems from hydrodynamic facility constraints when examining large-scale deployments [18]. Within finite wave tank dimensions, array upscaling necessitates geometric similitude compromises that frequently distort hydrodynamic scaling laws. Moreover, systematic wave generation inaccuracies inherent in many experimental facilities propagate measurement uncertainties, particularly compromising experimental validity for small-scale WEC configurations [19]. The prohibitively expensive infrastructure requirements for large-scale wave basin construction and sea trials further restrict physical experimentation. Consequently, contemporary wave farm research predominantly employs computationally driven approaches through numerical modeling and mathematical frameworks [20].

In traditional numerical simulation studies, the wave-structure interaction is typically evaluated based on potential flow theory, Navier-Stokes equations, or rapid calculation methods, e.g., radiation-potential approximations [21], the Morison equation [22], and machine learning [23]. Among these, significant simplifications are made in the rapid calculation methods, e.g., in the study by [21], the calculation of large arrays containing 1000 WECs considered the effects of incident and diffracted waves, neglecting the influence of radiation waves generated by each WEC. In calculations based on the Morrison equation, the accuracy is constrained by the influence of the float's geometric shape and dimensions, especially for floats with a small length-to-width ratio [24, 25]. Therefore, traditional methods based on potential flow theory and Navier-Stokes equations tend to provide more accurate evaluations. However, the application of computational fluid dynamics (CFD) methodologies for analyzing large-scale array configurations proves prohibitively computationally intensive due to the inherent complexity of solving Navier-Stokes equations at relevant scales. Consequently, CFD-based investigations remain virtually absent from the literature concerning expansive wave energy farms, with existing studies predominantly focusing on individual or reduced-scale array configurations [26, 27]. Thus, research on array-based WECs based on potential flow theory strikes a balance between accuracy and efficiency [28]. In this approach, the diffraction and radiation potentials are derived from the incident

wave potential, incorporating the boundary conditions of the structure and the continuity conditions of the fluid [29]. The wave field's velocity potential is derived through linear superposition principles within potential flow theory, with boundary element method (BEM) implementations—as featured in commercial platforms such as ANSYS AQWA [30], WAMIT [31], FAST [32], and HydroSTAR [33]—serving as prevalent computational frameworks. However, critical limitations emerge when employing these tools for hydrodynamic coefficient analysis in multi-body WEC arrays. Software-imposed mesh generation constraints restrict both the total number of discretized elements and their distribution across array components. For instance, according to the ANSYS AQWA Theory Manual (Release 2025 R1, Section 5.3) [30], under typical configurations, AQWA simulations are constrained by a practical mesh limit of approximately 40,000 surface elements, which can necessitate under-resolved meshes (e.g., ≤ 400 elements per device in 100-unit arrays) and potentially reduce hydrodynamic accuracy [8]. These spatial resolution considerations also limit the representable spectral bandwidth, particularly for short-wavelength simulations. Moreover, while SWAN is widely adopted for large-scale spectral wave field modeling, it is not typically designed for coupled array-scale fluid–structure interaction (FSI) optimization, as outlined in the SWAN User Manual (Version 41.51, Section 2) [34, 35].

In terms of mathematical analysis, substantial progress has been made over several decades in evaluating FSI problems. Mathematical modeling provides not only a flexible and physically transparent framework but also convenient pathways for coupling with control, optimization, and multi-physics simulations [36]. The analytical foundations of multi-body hydrodynamics were laid by Kagemoto and Yue [37], who proposed an exact algebraic interaction formulation capable of predicting diffraction and radiation coupling among multiple three-dimensional bodies within the context of linear potential flow. This work, together with the large-spacing radiation approximation of Williams and Abul-Azm [38], significantly advanced the theoretical understanding and computational tractability of multi-body interactions. Subsequent developments, such as the Fourier–Bessel and Graf's-addition formulations by Siddorn and Eatock Taylor [39], extended these principles to truncated and floating cylinder arrays, enabling more precise estimation of added mass, radiation damping, and excitation forces for array configurations. More recently, Zeng et al. [40, 41] generalized this class of analytical models to multi-degree-of-freedom (DOF) systems, allowing for relative motions among array members and revealing the sensitivity of hydrodynamic responses and energy-capture characteristics to coupled DOFs.

Building upon these theoretical advances, the present study applies the eigenfunction-expansion and Graf's-addition methods to derive the diffraction and radiation potentials under multi-body interaction, explicitly incorporating PTO damping, stiffness, and mooring effects. The unknown coefficients of the potential functions are solved by enforcing fluid continuity across domain interfaces, yielding a compact analytical framework capable of predicting the dynamic behavior of both floating and submerged WEC arrays with high computational efficiency. The diffraction and radiation potential solutions for truncated cylindrical arrays were further refined by Child and Venugopal [42], who expanded the velocity potential through eigenfunction series following Yeung [43]'s methodology. This structural configuration inherently partitions the fluid domain into interior and exterior subregions, thereby constraining geometric adaptability of submerged components to the vertical truncated cylinder. Notably, the analytical framework developed in Child and Venugopal [42]'s study incorporates optimization algorithms, enabling rapid frequency-domain dynamic response computation for WECs. Such methodology significantly accelerates fitness value determination, thereby enhancing multi-parameter optimization capabilities as demonstrated in Zhu et al. [23], Zeng et al. [44]. Furthermore, an innovative analytical framework for hybrid wave farm assessment was developed by Zheng et al. [45, 46, 47], which pioneers the simultaneous incorporation of both FB and oscillating water column (OWC) devices. This groundbreaking work constitutes the first successful integration of multi-type WEC technologies within a unified computational model. Based on this concept, Zhu et al. [48, 49] developed an analytical model for a wind-wave hybrid system, which can be used to calculate coupled systems and co-located systems consisting of array-based floating offshore wind turbines (FOWTs) and FB WECs, providing an effective computational method for ongoing FOWT projects. Given the importance of considering structural flexibility in certain FSI problems, advancing beyond rigid-body assumptions, Renzi et al. [50], Michele et al. [51, 52], and Li et al. [53] developed a transformative potential flow solution for deformable disc structures, enabling full-field motion quantification that has redefined flexible WEC design paradigms. This theoretical framework facilitates precise motion response prediction at arbitrary points on deformable structures, significantly advancing research on flexible marine structures [54, 55]. While inherently limited in nonlinear hydrodynamic resolution compared to CFD, analytical approaches have evolved through weakly nonlinear formulations by Michele et al. [56, 57], Li [58], and Wang and Liu [59], particularly addressing wave transformation and WEC

interaction dynamics. The contribution most pertinent to current investigations emerges from the analytical model established by Zhu et al. [8], which enables precise hydrodynamic computation and coupled dynamic assessment for multi-component floating systems employing composite cylindrical configurations. In the case study, the FSI problem of a system containing OC4-DeepcWind FOWTs and floating photovoltaics (FPVs) was investigated, where the coupled motion equations were formulated by incorporating rigid and articulated constraints to evaluate the motion responses of FOWTs and FPVs in the farm. Additionally, in our previous modeling [8], the number of floats with composite shapes N=84, each containing three internal water regions and one external public water region (i.e., a total of $3N + 1$ water regions). This methodology suggests computational feasibility for the present investigation, where the FB structure contains $N + 1$ water regions and the CETO structure contains $2N + 1$ water regions, it may be feasible to compute wave farms with $N > 100$.

Hence, this study fills the gap in comparative research between array-based CETO and FB systems, potentially catalyzing renewed interest in the CETO system and further validating its engineering application potential. Methodologically, the study employs the eigenfunction matching method, Fourier series method, and multi-body Graf's addition to evaluate the wave-structure interaction by solving the diffraction and radiation potentials, and integrated with the coupled equation of motion to investigate the energy capture and kinematic response characteristics of the array-based CETO and FB systems. After running the convergence analysis and model validation, the present model is employed to perform a multimode impact analysis. Case studies clearly reveal the effects of PTO damping, stiffness, geometric dimensions, and submergence depth on the wave energy capture efficiency, bandwidth, and peak frequency of the CETO system. Notably, a comparative analysis between FB and CETO systems reveals pronounced disparities in wave-energy-harvesting efficacy between isolated and array configurations, clarifying the performance of array-based CETO systems. The paper is organized as follows: Section 2 details the mathematical framework governing multi-body hydrodynamic interactions and coupled system dynamics. Convergence analysis and model validation are described in Section 3. A multiparametric analysis is conducted using the validated model, with the results and discussions provided in Section 4. Concluding remarks in Section 5 synthesize key findings and outline future research trajectories for enhanced CETO system development.

2. Mathematical model

In the model, an array of FB and CETO devices is considered. Each WEC includes a three-tether mooring and PTO system to make motion controllable and capture wave energy, as shown in Fig 2. For the three-tethered device [60], the tethers are evenly distributed around the buoy, forming an angle of $\alpha_h = 120^\circ$ between them, directed toward the center of gravity, and inclined at an angle α_v to the vertical. To study the hydrodynamic performance of the array-based FB and CETO WECs, the two systems are defined as Type 1 and Type 2, containing N vertically truncated cylinders (i.e., index $n = 1, 2, \cdots, N$).

A Cartesian coordinate system $Oxyz$ is used, with the Oxy plane at the still water level (SWL) $z = 0$ and z axis pointing upward. To study each float in the array, a local coordinate system (r_n, θ_n, z) and rotation centre $(r_n = 0,\ z = z_n)$ needs to be defined, corresponding to the local Cartesian coordinate system (x_n, y_n, z) [61]. According to the established coordinate system, the radius of each WEC is denoted as $R^{(n)}$, the thickness as $d_t^{(n)}$, and the submergence depth as $d_s^{(n)}$ (i.e., for the FB, $d_s^{(n)}$ is absent and $z_n = 0$, whereas for the CETO, $d_s^{(n)} + d_t^{(n)}/2 = -z_n$), as shown in Fig. 2. To simplify the expression, we can define the draft depth is $d_1^{(n)}$ for FB, and for CETO, $d_1^{(n)} = d_s^{(n)}$ and $d_2^{(n)} = d_s^{(n)} + d_t^{(n)}$. The fluid is divided as follows: (a) an external fluid domain, extending horizontally to infinity, denoted as region Ω_0 (i.e., $r_n \geq R^{(n)}, -h \leq z \leq 0$ for $n = 1, 2, \cdots, N$); (b) fluid domains beneath the column, denoted as region Ω_1^n (i.e., $0 \leq r_n \leq R^{(n)}, -h \leq z \leq -d_1^{(n)}$ for FB and $-h \leq z \leq -d_2^{(n)}$ for CETO, $n = 1, 2, \cdots, N$); (c) fluid domains beneath the free water surface and above the column, denoted as region Ω_2^n (i.e., $0 \leq r_n \leq R^{(n)}, -d_1^{(n)} \leq z \leq 0$ for CETO, $n = 1, 2, \cdots, N$), where h denotes the depth of water.

2.1. Governing equation and boundary conditions

The present problem is addressed within the framework of potential flow theory, assuming that the flow is inviscid, incompressible and irrotational. The floats are exposed to a monochromatic incident wave and can oscillate independently in six degrees of freedom. To represent the motion of fluid particles, we utilize a velocity potential expressed as $\Phi(x, y, z, t) = \mathrm{Re}[\phi(x, y, z)e^{-\mathrm{i}\omega t}]$, where ϕ denotes the complex spatial velocity potential, Re indicates the real part of

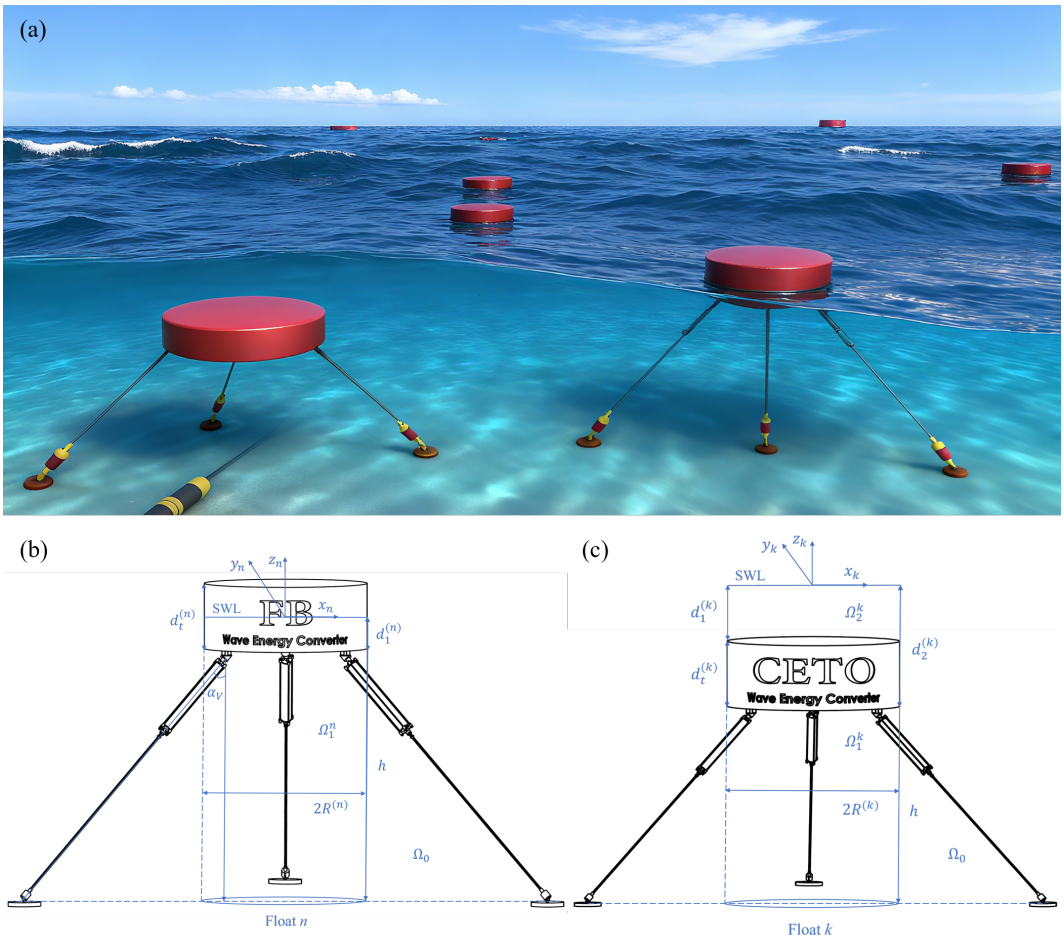

Fig. 2. WECs array for FB and CETO systems.

the argument, i represents the imaginary unit, and t is time. Based on the approach of Evans [62], the complex spatial velocity potential can be decomposed as $\phi = \phi_I + \phi_D + \sum_{p=1}^{N}\sum_{i=1}^{6} \dot{A}_p^i \phi_{p,i}$, where ϕ_I is the incident wave potential, ϕ_D is the diffraction potential, and $\phi_{p,i}$ is the radiation potential for the float p in the i-th mode of the velocity amplitude $\dot{A}_p^i$ ($i = 1 \sim 6$, representing surge, sway, heave, roll, pitch, and yaw, respectively).

Adopting the theoretical framework established in Mei et al. [63], the spatial velocity potential governing unperturbed incident wave fields can be formulated as:

$$\phi_I(r_n, \theta_n, z) = -\frac{\mathrm{i}gA}{\omega}\frac{\cosh\left[k_0\left(z+h\right)\right]}{\cosh\left(k_0 h\right)} e^{\mathrm{i}k_0(x_n\cos\beta + y_n\sin\beta)} \times \sum_{m=-\infty}^{\infty} \mathrm{i}^m e^{-\mathrm{i}m\beta} J_m\left(k_0 r_n\right) e^{\mathrm{i}m\theta_n}, \tag{1}$$

where A denotes wave amplitude, ω the angular frequency, β the propagation angle relative to the x-axis, k_0 the wavenumber, and J_m the mth order Bessel function of the first kind. The acceleration of gravity is denoted by g.

To solve for the spatial velocity potential, we consider that it satisfies the free-surface boundary and the body-boundary condition:

$$\frac{\partial \phi_\chi}{\partial z} = \frac{\omega^2}{g}\phi_\chi, \ z = 0, \ \chi = \text{`}D\text{'} \ \text{ or } \ \text{`}p,i\text{'} \tag{2}$$

$$\frac{\partial \phi_\chi}{\partial z} = 0, \quad z = -h, \quad \chi = \text{`}D\text{'} \text{ or } \text{`}p, i\text{'}, \tag{3}$$

$$\frac{\partial \phi_I}{\partial z} = -\frac{\partial \phi_D}{\partial z}, \quad z = -d_q^{(n)}, \quad r_n \le R^{(n)} \text{ for } q = 1, 2, \tag{4}$$

$$\frac{\partial \phi_I}{\partial r_n} = -\frac{\partial \phi_D}{\partial r_n}, \quad -d_q^{(n)} \le z \le -d_{q-1}^{(n)}, \quad r_n = R^{(n)} \text{ for } q = 1, 2, \tag{5}$$

$$\frac{\partial \phi_{p,i}}{\partial z} = \delta_{n,p}(\delta_{3,i} + \delta_{4,i} r_n \sin\theta_n - \delta_{5,i} r_n \cos\theta_n), z = -d_q^{(n)}, \quad r_n \le R^{(n)} \text{ for } q = 1, 2, \tag{6}$$

$$\frac{\partial \phi_{p,i}}{\partial r_n} = \delta_{n,p}(\delta_{1,i}\cos\theta_n + \delta_{2,i}\sin\theta_n - \delta_{4,i}(z - z_n)\sin\theta_n + \delta_{5,i}(z - z_n)\cos\theta_n), \quad -d_q^{(n)} \le z \le -d_{q-1}^{(n)}, \quad r_n = R^{(n)} \text{ for } q = 1, 2, \tag{7}$$

where $d_0^{(n)} = 0$; $\delta_{n,p}$ represents the Kronecker delta function.

2.2. Expression of the velocity potential

The spatial velocity potential in the exterior region Ω_0 can be expressed as [64, 55]

$$\phi_\chi^{(0,n)} = \sum_{n=1}^{N} \sum_{m=-\infty}^{\infty} \sum_{j=0}^{\infty} A_{m,j}^{\chi,n} H_m(k_j r_n) \cosh[k_j(z + h)] e^{\mathrm{i}m\theta_n}, \tag{8}$$

where χ = 'D' or 'p, i', and $A_{m,j}^{\chi,n}$ represent the unknown coefficients. The Hankel function of the first kind of order m is denoted by H_m (i.e., $H_m(\cdot) = J_m(\cdot) + \mathrm{i}Y_m(\cdot)$). Here, $k_0 \in \mathbb{R}^+$ corresponds to propagating waves, while $k_j \in i\mathbb{R}^+$ for $j = 1, 2, 3, \ldots$ represent evanescent waves. The values k_0 and k_j are derived from the dispersion relation $\omega^2 = g k_j \tanh(k_j h)$ for the external region, where k_0 is the positive real root and k_j are the infinite positive imaginary roots.

Applying Graf's addition theorem for Bessel functions [65], $\phi_\chi^{(0,n)}$ can be reformulated in local coordinates:

$$\begin{aligned} \phi_\chi^{(0,n)}(r_n, \theta_n, z) = & \sum_{m=-\infty}^{\infty} \sum_{j=0}^{\infty} A_{m,j}^{\chi,n} H_m(k_j r_n) \cosh[k_j(z + h)] e^{\mathrm{i}m\theta_n} \\ & + \sum_{\substack{k=1 \\ k\neq n}}^{N} \sum_{m=-\infty}^{\infty} \sum_{j=0}^{\infty} A_{m,j}^{\chi,k} \cosh[k_j(z + h)] \sum_{m'=-\infty}^{\infty} H_{m-m'}^{(1)}(k_j R_{nk}) J_{-m'}(k_j r_n) e^{\mathrm{i}(m\theta_{kn} - m'\theta_{nk})} e^{\mathrm{i}m'\theta_k}, \end{aligned} \tag{9}$$

where R_{nk} represents the distance between the centers of cylinders n and k (with $r_n < R_{nk}$); θ_{nk} is the angle at cylinder n between the positive x-axis and the line connecting the centers of cylinders n and k, measured counter-clockwise, and θ_{kn} is the angle between the line $O_k O_n$ and the positive x-axis [42], as shown in Fig. 3.

In the region Ω_1^n,

$$\phi_\chi^{(1,n)}(r_n, \theta_n, z) = \sum_{m=-\infty}^{\infty} \left\{ \frac{B_{m,0}^{\chi,n}}{\sqrt{2}} \left(\frac{r_n}{R^{(n)}} \right)^{|m|} + \sum_{j=1}^{\infty} B_{m,j}^{\chi,n} \frac{I_m\left(k_{1,j}^{(n)} r_n\right)}{I_m\left(k_{1,j}^{(n)} R^{(n)}\right)} \cos\left[k_{1,j}^{(n)}(z + h)\right] \right\} e^{\mathrm{i}m\theta} + \phi_{\chi,S}^{(1,n)}(r_n, \theta_n, z), \tag{10}$$

where $B_{m,j}^{\chi,n}$ are unknown coefficients; $k_{1,j}^{(n)} = j\pi/(h - d_q^{(n)})$ $(j = 0, 1, 2 \ldots)$; $\phi_{\chi,S}^{(1,n)}$ is a particular solution in Region Ω_1^n,

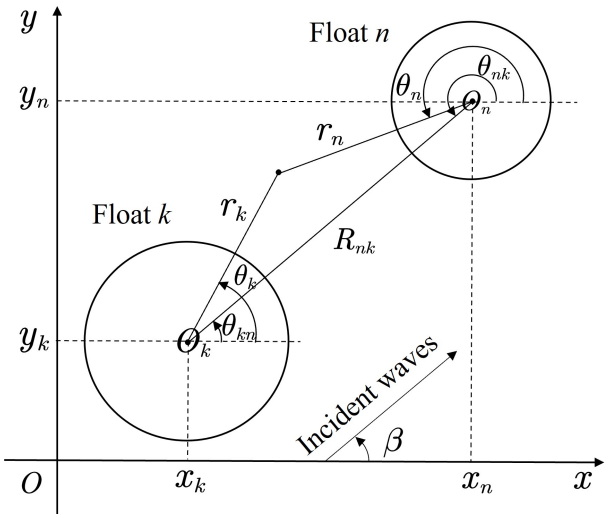

Fig. 3. Definition sketch for a multiple-member float (plan view).

which for $\chi =$ 'D' , $\phi_{\chi,S}^{(1,n)} = -\phi_I$; for $\chi =$ 'p, i' and $n \neq p$, $\phi_{\chi,S}^{(1,n)} = 0$; for $\chi =$ 'p, i' and $n = p$,

$$\phi_{\chi,S}^{(1,n)}(r_n, \theta_n, z) = \begin{cases} 0, & i = 1, 2, 6 \\ \frac{1}{4\left(h-d_q^{(n)}\right)}\left[2(z+h)^2 - {r_n}^2\right], & i = 3 \\ \frac{\sin\theta_n}{8\left(h-d_q^{(n)}\right)}\left[4r_n(z+h)^2 - {r_n}^3\right], & i = 4 \\ \frac{-\cos\theta_n}{8\left(h-d_q^{(n)}\right)}\left[4r_n(z+h)^2 - {r_n}^3\right], & i = 5 \end{cases}, \tag{11}$$

$q = 1$ for floating structure and $q = 2$ for submerged structure.

In the region Ω_2^n,

$$\phi_{\chi}^{(2,n)}(r_n, \theta_n, z) = \sum_{m=-\infty}^{\infty}\sum_{j=0}^{\infty} C_{m,j}^{\chi,n} J_m(k_{2,j}^{(n)} r_n)\cosh[k_{2,j}^{(n)}(z + d_1^{(n)})]e^{\mathrm{i}m\theta_n} + \phi_{\chi,S}^{(2,n)}(r_n, \theta_n, z), \tag{12}$$

where $C_{m,j}^{\chi,n}$ are the unknown coefficients to be determined; $k_{2,0}^{(n)}$ and $k_{2,j}^{(n)}$ for $j = 1, 2, 3, ...$ correspond to the positive real root and the infinite positive imaginary roots of the dispersion relation $\omega^2 = gk_{2,j}^{(n)}\tanh(k_{2,j}^{(n)}d_2^{(n)})$. The function $\phi_{\chi,S}^{(2,n)}$ represents a particular solution in the region Ω_2^n, which can be expressed as: for $\chi =$ 'D', $\phi_{\chi,S}^{(2,n)} = -\phi_I$; for $\chi =$ 'p, i' and $n \neq p$, $\phi_{\chi,S}^{(2,n)}$ equals 0, while for $n = p$, $\phi_{\chi,S}^{(2,n)}$ can be written as

$$\phi_{\chi,S}^{(2,n)}(r_n, \theta_n, z) = \begin{cases} 0, & i = 1, 2, 6 \\ z + \frac{g}{\omega^2}, & i = 3 \\ r_n \sin\theta_n\left(z + \frac{g}{\omega^2}\right), & i = 4 \\ -r_n\cos\theta_n\left(z + \frac{g}{\omega^2}\right), & i = 5 \end{cases}. \tag{13}$$

2.3. Solution of the unknown coefficient

The continuity conditions of pressure and flux across the boundaries between the interior and exterior domains are essential for determining the unknown coefficients in the spatial potentials.

(i) Continuity of pressure at the boundary $r_n = R^{(n)}$, $-h \leq z \leq -d_q^{(n)}$ ($q = 1$ for floating structure and $q = 2$ for submerged structure):

$$\phi_{\chi}^{(0,n)} = \phi_{\chi}^{(1,n)}, \ \chi =\text{'}D\text{'} \text{ and } \text{'}p, i\text{'}. \tag{14}$$

Inserting Eqs. (9) and (10) into Eq. (14), after multiplying both sides by $\cosh\left[k_{1,\zeta}^{(n)}\left(z+d_q^{(n)}\right)\right]e^{-\mathrm{i}\tau\theta_n}$ and integrating for $z\in\left[-h,-d_q^{(n)}\right]$ and $\theta_n\in[0,2\pi]$, for any pair of integers (ζ,τ), it can be shown that

$$\begin{aligned}&\sum_{j=0}^{\infty}A_{\tau,j}^{\chi,n}\Pi_{j,\iota}^{0,2,n}(h,d_q^{(n)})+\sum_{\substack{k=1\\k\neq n}}^{N}\sum_{m=-\infty}^{\infty}\sum_{j=1}^{\infty}A_{m,j}^{\chi,n}T_{m,j}^{\tau,k,n}\Pi_{j,\iota}^{0,2,n}(h,d_q^{(n)})\\&=\frac{gA\mathrm{i}^{\tau+1}I_ne^{-\mathrm{i}\tau\beta}}{\omega\cosh(k_0h)}J_\tau\left(k_0R^{(n)}\right)\Pi_{0,\iota}^{0,2,n}(h,d_q^{(n)})+B_{\tau,j}^{\chi,n}\Pi_{\zeta,\zeta}^{\prime 2,2,n}(h,d_q^{(n)}),\end{aligned}\tag{15}$$

where

$$T_{m,j}^{\tau,k,n}=\frac{H_{m-\tau}\left(k_{q,j}^{(n)}R_{nk}\right)J_{-\tau}\left(k_{q,j}^{(n)}R^{(n)}\right)e^{\mathrm{i}(m\theta_{kn}-\tau\theta_{nk})}}{H_{m-\tau}\left(k_{q,j}^{(n)}R^{(n)}\right)}\tag{16}$$

$$\Pi_{j,\zeta}^{q,\iota,n}(\alpha,\beta)=\int_{-\alpha}^{-\beta}Z_{q,n}^{(n)}(z)\cosh\left[k_{\iota,\zeta}^{(n)}\left(z+d_\iota^{(n)}\right)\right]dz=$$
$$\begin{cases}\frac{1}{\left(k_{q,j}^{(n)}\right)^2+\left(k_{\iota,\zeta}^{(n)}\right)^2}\left\{k_{q,j}^{(n)}\sinh\left[k_{q,j}^{(n)}\left(z+d_q^{(n)}\right)\right]\cosh\left[k_{\iota,\zeta}^{(n)}\left(z+d_\iota^{(n)}\right)\right]\right.\\\qquad\left.+k_{\iota,\zeta}^{(n)}\cosh\left[k_{q,j}^{(n)}\left(z+d_q^{(n)}\right)\right]\times\mathrm{i}\sinh\left[k_{\iota,\zeta}^{(n)}\left(z+d_\iota^{(n)}\right)\right]\right\}\Big|_{-\alpha}^{-\beta}, & \text{for } j=0;\\ \frac{1}{2}\left\{\frac{\mathrm{i}\sinh\left[k_{q,j}^{(n)}\left(z+d_q^{(n)}\right)+k_{\iota,\zeta}^{(n)}\left(z+d_\iota^{(n)}\right)\right]}{k_{q,j}^{(n)}+k_{\iota,\zeta}^{(n)}}+\frac{\mathrm{i}\sinh\left[k_{q,j}^{(n)}\left(z+d_q^{(n)}\right)-k_{\iota,\zeta}^{(n)}\left(z+d_\iota^{(n)}\right)\right]}{k_{q,j}^{(n)}-k_{\iota,\zeta}^{(n)}}\right\}\Big|_{-\alpha}^{-\beta}, & \text{for } k_{q,j}^{(n)}\neq k_{\iota,\zeta}^{(n)},\ j>1;\\ \frac{1}{4k_{\iota,\zeta}^{(n)}}\left\{2k_{\iota,\zeta}^{(n)}z\cosh\left[k_{\iota,\zeta}^{(n)}\left(d_\iota^{(n)}-d_q^{(n)}\right)\right]+\mathrm{i}\sinh\left[k_{\iota,\zeta}^{(n)}\left(2z+d_\iota^{(n)}+d_q^{(n)}\right)\right]\right\}\Big|_{-\alpha}^{-\beta}, & \text{for } k_{q,j}^{(n)}=k_{\iota,\zeta}^{(n)}\ j>1;\end{cases}\tag{17}$$

where $d_0^{(n)}=h$ and $k_{0,j}^{(n)}=k_j$ for $n=1,2,3,...,N$, $j=0,1,2,....$ $\Pi_{j,\zeta}^{\prime q,\iota,n}(\alpha,\beta)=\Pi_{j,\zeta}^{q,\iota,n}(\alpha,\beta)$ for $j>1$; $\Pi_{j,\zeta}^{\prime q,\iota,n}(\alpha,\beta)=\frac{\sin[k_{q,j}^{(n)}(\alpha-\beta)]}{\sqrt{2}k_{q,j}^{(n)}\cos(k_{q,j}^{(n)}\alpha)}$ for $j=0$.

(ii) Continuity of pressure at the boundary $r_n=R^{(n)}$, $-d_1^{(n)}\le z\le 0$:

$$\phi_\chi^{(0,n)}=\phi_\chi^{(2,n)},\quad \chi=\text{`}D\text{'}\ \text{ and }\ \text{`}p,i\text{'}.\tag{18}$$

Inserting Eqs. (9) and (12) into Eq. (18), after multiplying both sides by $\cosh\left[k_{2,\zeta}^{(n)}\left(z+d_1^{(n)}\right)\right]e^{-\mathrm{i}\tau\theta_n}$ and integrating for $z\in\left[-d_1^{(n)},0\right]$ and $\theta_n\in[0,2\pi]$, for any pair of integers (ζ,τ), we get:

$$\begin{aligned}&\sum_{j=0}^{\infty}A_{\tau,j}^{\chi,n}\Pi_{j,\iota}^{0,1,n}(d_1^{(n)},0)+\sum_{\substack{k=1\\k\neq n}}^{N}\sum_{m=-\infty}^{\infty}\sum_{j=1}^{\infty}A_{m,j}^{\chi,n}T_{m,j}^{\tau,k,n}\Pi_{j,\iota}^{0,1,n}(d_1^{(n)},0)\\&=\frac{gA\mathrm{i}^{\tau+1}I_ne^{-\mathrm{i}\tau\beta}}{\omega\cosh(k_0h)}J_\tau\left(k_0R^{(n)}\right)\Pi_{0,\iota}^{0,1,n}(d_1^{(n)},0)-C_{\tau,j}^{\chi,n}\Pi_{\zeta,\zeta}^{1,1,n}(d_1^{(n)},0).\end{aligned}\tag{19}$$

(iii) Continuity of velocity at the boundary $r_n = R^{(n)}$: for floating structure,

$$\frac{\partial\phi_\chi^{(0,n)}}{\partial r_n} = \begin{cases} \begin{cases} -\frac{\partial\phi_I}{\partial r_n}, & \chi = \text{`}D\text{'} \\ \delta_{n,p}\begin{bmatrix} \delta_{1,i}\cos\theta_n + \delta_{2,i}\sin\theta_n \\ -\delta_{4,i}(z-z_n)\sin\theta_n \\ +\delta_{5,i}(z-z_n)\cos\theta_n \end{bmatrix}, & \chi = \text{`}p,i\text{'} \end{cases}, & \text{for } -d_1^{(n)} \le z \le 0; \\ \frac{\partial\phi_\chi^{(1,n)}}{\partial r_n}, \ \chi = \text{`}D\text{' and `}p,i\text{'}, & \text{for } -h \le z \le -d_1^{(n)}. \end{cases} \tag{20}$$

Inserting Eqs. (9),(10) into Eq. (20), after multiplying both sides by $\cos[k_0(z+h)]\,e^{-\mathrm{i}\tau\theta_n}$ and integrating for $z \in [-h,0]$ and $\theta_n \in [0,2\pi]$, for any pair of integers (ζ,τ), we get:

$$\begin{aligned} &-\frac{gA\mathrm{i}^{\tau+1}}{\omega\cosh(k_0h)} I_n e^{-\mathrm{i}\tau\beta}\left[\frac{\tau}{R^{(n)}}J_\tau\left(k_0R^{(n)}\right) - k_0J_{\tau+1}\left(k_0R^{(n)}\right)\right]\Pi_{0,\zeta}^{0,0,n}(h,0) \\ &+\sum_{j=0}^{\infty} A_{\tau,j}^{\chi,n}\Lambda_{0,j,0}^{\tau,1,n}\Pi_{\zeta,\zeta}^{0,0,n}(h,0) + \sum_{\substack{k=1\\k\neq n}}^{N}\sum_{m=-\infty}^{\infty} A_{\tau,j}^{\chi,n}T_{m,j}^{\tau,k,n}\Pi_{\zeta,\zeta}^{0,0,n}(h,0) \\ &=\sum_{j=0}^{\infty} B_{\tau,j}^{\chi,n}\Lambda_{2,j,2}^{\tau,1,n}\Pi'^{2,0,n}_{j,\zeta}(h,d_1^{(n)}); \end{aligned} \tag{21}$$

for submerged structure:

$$\frac{\partial\phi_\chi^{(0,n)}}{\partial r_n} = \begin{cases} \frac{\partial\phi_\chi^{(2,n)}}{\partial r_n}, \ \chi = \text{`}D\text{' and `}p,i\text{'}, & -d_1^{(n)} \le z \le 0; \\ \begin{cases} -\frac{\partial\phi_I}{\partial r_n}, & \chi = \text{`}D\text{'} \\ \delta_{n,p}\begin{bmatrix} \delta_{1,i}\cos\theta_n + \delta_{2,i}\sin\theta_n \\ -\delta_{4,i}(z-z_n)\sin\theta_n \\ +\delta_{5,i}(z-z_n)\cos\theta_n \end{bmatrix}, & \chi = \text{`}p,i\text{'} \end{cases}, & \text{for } -d_2^{(n)} \le z \le -d_1^{(n)}; \\ \frac{\partial\phi_\chi^{1,n)}}{\partial r_n}, \ \chi = \text{`}D\text{' and `}p,i\text{'}, & \text{for } -h \le z \le -d_2^{(n)}. \end{cases} \tag{22}$$

Inserting Eqs. (9),(10) and (12) into Eq. (22), after multiplying both sides by $\cos[k_0(z+h)]\,e^{-\mathrm{i}\tau\theta_n}$ and integrating for $z \in [-h,0]$ and $\theta_n \in [0,2\pi]$, for any pair of integers (ζ,τ), we get:

$$\begin{aligned} &-\frac{gA\mathrm{i}^{\tau+1}}{\omega\cosh(k_0h)} I_n e^{-\mathrm{i}\tau\beta}\left[\frac{\tau}{R^{(n)}}J_\tau\left(k_0R^{(n)}\right) - k_0J_{\tau+1}\left(k_0R^{(n)}\right)\right]\Pi_{0,\zeta}^{0,0,n}(h,0) + \sum_{j=0}^{\infty} A_{\tau,j}^{\chi,n}\Lambda_{0,j,0}^{\tau,1,n}\Pi_{\zeta,\zeta}^{0,0,n}(h,0) \\ &+\sum_{\substack{k=1\\k\neq n}}^{N}\sum_{m=-\infty}^{\infty} A_{\tau,j}^{\chi,n}T_{m,j}^{\tau,k,n}\Pi_{\zeta,\zeta}^{0,0,n}(h,0) = \sum_{j=0}^{\infty} B_{\tau,j}^{\chi,n}\Lambda_{2,j,2}^{\tau,1,n}\Pi'^{2,0,n}_{j,\zeta}(h,d_2^{(n)}) + \sum_{j=0}^{\infty} C_{\tau,j}^{\chi,n}\Lambda_{1,j,0}^{\tau,1,n}\Pi_{j,\zeta}^{1,0,n}(d_1^{(n)},0), \end{aligned} \tag{23}$$

where

$$T'^{\tau,k,n}_{m,j} = \frac{H_{m-\tau}\left(k_{q,j}^{(n)}R_{nk}\right)}{H_m\left(k_{q,j}^{(n)}R^{(n)}\right)}\left[\frac{-\tau}{R^{(n)}}J_{-\tau}\left(k_{q,j}^{(n)}R^{(n)}\right) - k_0J_{-\tau+1}\left(k_{q,j}^{(n)}R^{(n)}\right)\right]e^{\mathrm{i}(m\theta_{kn}-\tau\theta_{nk})}, \tag{24}$$

$$\Lambda_{q,j,u}^{\tau,\varepsilon,n} = \begin{cases} \frac{\tau}{R^{(n)}} + \frac{(-1)^{\gamma_2(\varepsilon-1)j}k_{q,j}^{(n)}V_{\tau+1}^{(\varepsilon)}\left(k_{q,j}^{(n)}R^{(n)}\right)}{V_\tau^{(\varepsilon)}\left(k_{q,j}^{(n)}R^{(n)}\right)}, & \text{others} \\ \gamma_{\delta_{j,\tau}}\frac{|\gamma_\tau|}{R^{(n)}}, & q=2, j=0, u=1 \\ \frac{|\tau|}{R^{(n)}}, & q=2, j=0, u=2 \end{cases} \tag{25}$$

$V_m^{(\varepsilon)} = H_m$ for $\varepsilon = 1$ and $V_m^{(\varepsilon)} = J_m$ for $\varepsilon = 2$; $\gamma_x = -1$ for $x = 0$ and $\gamma_x = x$ for $x \neq 0$.

In the solution process, the potential function in region Ω_2^n does not exist for the floating structure. Therefore, the unknown coefficients $A_{m,j}^{\chi,n}$ and $B_{m,j}^{\chi,n}$ can be determined by combining Eqs. (15) and (21). For submerged structures, the aforementioned potential functions exist, and the unknown coefficients $A_{m,j}^{\chi,n}$, $B_{m,j}^{\chi,n}$, and $C_{m,j}^{\chi,n}$ must be solved by applying Eqs. (15), (19), and (23). The infinite series $e^{-\mathrm{i}m\theta_n}$ and $Z_{q,j}^{(n)}$ are truncated at $m = M$ and $j = J$, respectively. Furthermore, analogous expressions for the radiation spatial potentials induced by six-degree-of-freedom oscillations of the floating array can be formulated. Analysis shows that both diffracted and radiation potentials utilize an identical linear complex coefficient matrix of dimensions $M \times J$, demonstrating that wave diffraction and radiation problems can be solved concurrently within this unified framework.

2.4. Wave excitation and hydrodynamic coefficients

When the hybrid system is subjected to the waves, the generalised force on cylinder n in mode i' ($i' = 1 \sim 6$ represent surge, sway, heave, roll, pitch, and yaw, respectively) can be calculated from $\mathrm{Re}[F_\chi^{n,i'}]$.

For floating structure,

$$F_\chi^{n,i'} = \mathrm{i}\omega\rho \int_0^{2\pi} \int_{-d_1^{(n)}}^{0} R^{(n)} C_{i'} (\phi_I + \phi_\chi^{(0,n)}) dz d\theta_n, \quad i' = 1, 2 \tag{26}$$

$$F_\chi^{n,i'} = \mathrm{i}\omega\rho \int_0^{2\pi} \int_0^{R^{(n)}} (\phi_I + \phi_\chi^{(1,n)}) r_n dr_n \quad i' = 3, \tag{27}$$

$$F_\chi^{n,i'} = \mathrm{i}\omega\rho \int_0^{2\pi} \left\{ \int_{-d_1^{(n)}}^{0} R^{(n)} C_{i'} (\phi_I + \phi_\chi^{(0,n)}) (z - z_n) dz - D_{i'} \int_0^{R^{(n)}} (\phi_I + \phi_\chi^{(1,n)}) r_n dr_n \right\} d\theta_n, \quad i' = 4, 5. \tag{28}$$

For submerged structure,

$$F_\chi^{n,i'} = \mathrm{i}\omega\rho \int_0^{2\pi} \int_{-d_2^{(n)}}^{-d_1^{(n)}} R^{(n)} C_{i'} (\phi_I + \phi_\chi^{(0,n)}) dz d\theta_n, \quad i' = 1, 2, \tag{29}$$

$$F_\chi^{n,i'} = \mathrm{i}\omega\rho \int_0^{2\pi} \left\{ \int_0^{R^{(n)}} (\phi_I + \phi_\chi^{(1,n)}) r_n dr_n - \int_0^{R^{(n)}} (\phi_I + \phi_\chi^{(2,n)}) r_n dr_n \right\} d\theta_n, \quad i' = 3, \tag{30}$$

$$\begin{aligned} F_\chi^{n,i'} = \mathrm{i}\omega\rho \int_0^{2\pi} \Bigg\{ & \int_{-d_2^{(n)}}^{-d_1^{(n)}} R^{(n)} C_{i'} (\phi_I + \phi_\chi^{(0,n)}) (z - z_n) dz \\ & - D_{i'} \left[\int_0^{R^{(n)}} (\phi_I + \phi_\chi^{(1,n)}) r_n dr_n - \int_0^{R^{(n)}} (\phi_I + \phi_\chi^{(2,n)}) r_n dr_n \right] \Bigg\} d\theta_n, \quad i' = 4, 5, \end{aligned} \tag{31}$$

where

$$C_{i'} = \begin{cases} -\sin\theta_n, i' = 2, 4 \\ -\cos\theta_n, i' = 1, 5 \end{cases}, D_{i'} = \begin{cases} r_n \sin\theta_n, i' = 4 \\ r_n \cos\theta_n, i' = 5 \end{cases}; \tag{32}$$

$\chi =$ 'D' corresponds to the wave excitation force, while $\chi =$ 'p, i' represent the radiation force induced by the i-th mode oscillation of float p. The radiation force can be represented by the associated radiation added mass $a_{p,i}^{n,i'}$ and damping coefficient $b_{p,i}^{n,i'}$, as follows:

$$F_{p,i}^{n,i'} = \mathrm{i}\omega a_{p,i}^{n,i'} - b_{p,i}^{n,i'}. \tag{33}$$

2.5. The coupled motion equations

Zhou et al. [66, 67] developed a numerical framework to examine fully nonlinear wave interactions with buoyant structures and tension-leg platforms. Their findings indicate that nonlinear formulations become essential only when higher-order harmonic components, such as springing and ringing phenomena, exert substantial influence [68, 57]. In floating offshore engineering applications, linear methodologies are predominantly employed due to their expediency and computational efficiency in assessing hybrid system performance [69, 70, 71]. Therefore, the linear motion

equation is adopted for the analysis, albeit with limited applicability in extreme sea states. The governing dynamics are described by:

$$\left\{ -\omega^2 \left[\boldsymbol{M}_m + \boldsymbol{A}(\omega)\right] - \mathrm{i}\omega \left[\boldsymbol{B}(\omega) + \boldsymbol{B}_{pto}\right] + \boldsymbol{C}_s + \boldsymbol{K}_{pto} \right\} \boldsymbol{X} = \boldsymbol{F} \tag{34}$$

where the excitation force vector $\boldsymbol{F}$ comprises the spectral components of wave-induced forces on each floater, derived from Eqs. (26)-(31); $\boldsymbol{M}_m$ is the structure mass matrix; $\boldsymbol{X}$ is complex amplitude of displacement vectors for N structures; $\boldsymbol{A}(\omega)$ and $\boldsymbol{B}(\omega)$ are hydrodynamic added mass and damping matrix due to the radiation potential, given by Eq. (33); $\boldsymbol{B}_{pto}$ and $\boldsymbol{K}_{pto}$ are linear PTO damping and stiffness matrix of the system; $\boldsymbol{C}_s$ is the hydrostatic restoring matrix. According to Sergiienko et al. [60] and Rijnsdorp et al. [1] the damping and stiffness matrix in surge, heave and pitch mode can be expressed as:

$$\boldsymbol{B}_{pto} = \begin{bmatrix} \frac{3}{2}B_{pto}\sin^2\alpha_v & 0 & 0 \\ 0 & 3B_{pto}\cos^2\alpha_v & 0 \\ 0 & 0 & 0 \end{bmatrix}, \qquad \boldsymbol{K}_{pto} = \begin{bmatrix} K_{pto,11} & 0 & K_{pto,15} \\ 0 & K_{pto,33} & 0 \\ K_{pto,51} & 0 & K_{pto,55} \end{bmatrix}, \tag{35}$$

where

$$\begin{aligned} K_{pto,11} &= \frac{3\sin^2\alpha_v}{2}\left(K_{pto} + \frac{C_{pto}}{3l_0\cos\alpha_v}\right) - \frac{C_{pto}}{l_0\cos\alpha_v}, \qquad K_{pto,15} = K_{pto,51} = -\frac{C_{pto}d_t}{2l_0\cos\alpha_v}, \\ K_{pto,33} &= 3\cos^2\alpha_v\left(K_{pto} + \frac{C_{pto}}{3l_0\cos\alpha_v}\right) - \frac{C_{pto}}{l_0\cos\alpha_v}, \qquad K_{pto,55} = -\frac{C_{pto}d_t\left[d_t + 2l_0\cos\alpha_v(\cos^2\alpha_v + 1)\right]}{8l_0\cos^3\alpha_v}; \end{aligned} \tag{36}$$

$l_0 = (h - z_n - 0.5d_t)/\cos\alpha_v$ denotes the initial tether length; $C_{pto} = -((\rho V - M_m))/(3\cos\alpha_v)$ is the force that counteracts the hydrostatic force in an undisturbed position.

We assume that the time-averaged power $p_w^{(n)}$ extracted by float n can be obtained from the contribution of mechanical damping B_{pto}. When the complex velocity column vector $\dot{\boldsymbol{X}}$ of the float n is obtained, the time-averaged power output by WEC array can be directly calculated by [72, 73]

$$P_w = \frac{1}{2}\dot{\boldsymbol{X}}^{\dagger}\boldsymbol{B}_{pto}\dot{\boldsymbol{X}}, \tag{37}$$

where the superscript † denotes complex-conjugate transpose and $|\cdot|$ represents the norm of a vector. According to the studies by Falnes [72] and Sergiienko et al. [14], the maximum absorbed power by an axisymmetric body in monochromatic waves is $P_{max} = \gamma J/k_0$, where J is the wave-energy transport per unit frontage of the incident wave (i.e., $J = \rho g^2 D(kh)A^2/(4\omega)$, where $D(kh)$ represent the depth function); γ is a coefficient dependent on the oscillation mode of motion ($\gamma = 1$ for heave, $\gamma = 2$ for surge or pitch, and $\gamma = 3$ when the body oscillates in heave, surge and pitch simultaneously). In this paper, to clearly evaluate the wave energy capture efficiency of the WEC, the time-averaged power absorption as given in Eq. (37) can be rewritten in terms of the q factor (i.e., $q = P_w/P_{max}$) [74, 49]. Unless otherwise noted, the rest of this paper focuses on the WECs in the array being identical (i.e., $R^{(n)} = R$, $d_t^{(n)} = d_t$, $d_s^{(n)} = d_s$).

3. Model validation

Before employing the mathematical model for case-specific investigations, rigorous convergence analysis of the hydrodynamic model and validation of both motion response amplitude operators (RAOs) and energy capture efficacy within the dynamic response paradigm must be executed. For convergence verification, an analysis is conducted utilizing the largest configuration of the array examined in this study (i.e., $N = 36$) through established computational methodologies [75, 76]. Computational results indicate that the hydrodynamic coefficients vary by less than 1% once the angular and vertical modal truncation thresholds reach $M \geq 5$ and $J \geq 25$; therefore, truncation parameters of $M = 5$ and $J = 30$ are adopted for the angular and vertical eigenmodes in all subsequent analyses. To authenticate hydrodynamic computational fidelity, the present analytical solutions are benchmarked against submerged structural hydrodynamics documented by chao Jiang et al. [77, 78] (Fig. 4). Specifically, Fig. 4a juxtaposes surge, heave, and pitch wave excitation forces; Figs. 4b and 4c contrast radiation damping and added mass coefficients across these

modes. Observed concordance between present solutions and reference data validates methodological precision. Moreover, corroborating prior research [8, 48], the analytical framework demonstrates robust capability in resolving hydrodynamic coefficients for both floating and submerged array systems.

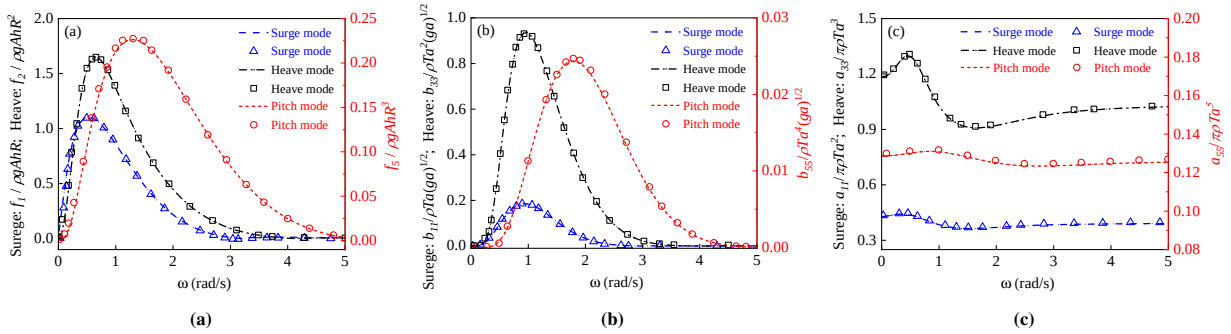

Fig. 4. Comparison of hydrodynamic coefficients of a submerged cylinder with thickness $d_t/R = 1.0$ at submerged depth $d_s/h = 0.25$ and water depth h/R=4: (a) wave force, (b) radiation damping, (c) added mass (Line: present analytical solution; dots: chao Jiang et al. [77, 78]).

Upon acquiring hydrodynamic coefficients, the dynamic response and energy harvesting efficiency of WECs may be determined via Eq. 34. Based on the work of Sergiienko et al. [14, 60], the dynamic response characteristics of two types of array-based WECs will be investigated in the linear framework. While linear kinematic frameworks are computationally expedient and extensively validated [48, 60], to ensure comprehensive analytical rigor, systematic validation of motion RAOs and energy extraction metrics is conducted for both floating and submerged WECs. Initially, validation of the FB motion RAO leveraged experimental data from a tri-floater physical model (Fig. 5), tested in a 60 m × 3 m wave basin with operational depth $h = 0.8$ m. The configuration employed three identical cylindrical floaters with $R/d = 0.5$, $d_t/R = 0.25$, and inter-body spacing $9R$. For parametric specifications and computational implementation details, consult Zhu et al. [23]. Fig. 5b demonstrates strong concordance among the present analytical model, the AMA-system, and experimental measurements, though minor overestimations by both computational models are observed. These deviations stem from the exclusion of viscous dissipation effects in the analytical and AMA frameworks. Crucially, under inviscid flow assumptions, the present model exhibits robust alignment with validated AMA-system results, confirming its efficacy in predicting motion responses of FB systems.

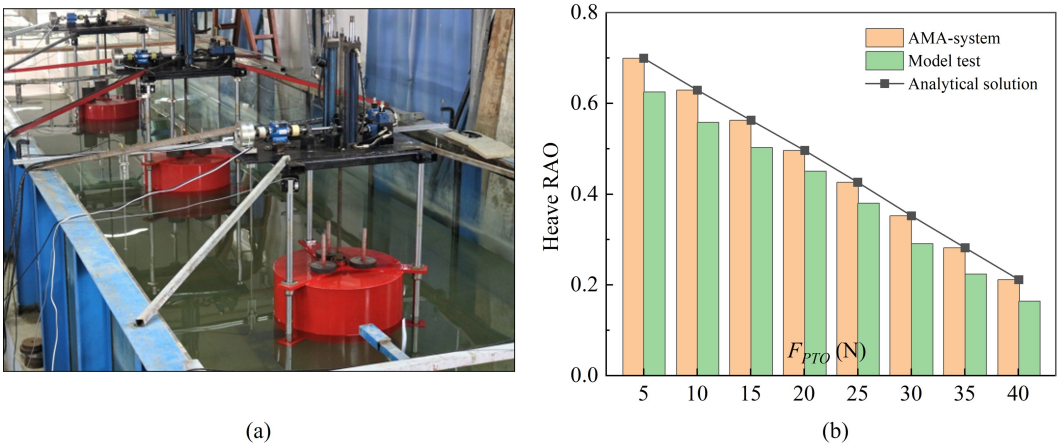

Fig. 5. Validation of FB WEC motion response: (a) tri-floater experimental configuration; (b) motion response characteristics for the forefloater adjacent to the wave generator. The experimental setup employs a 60 m × 3 m wave basin with an operational depth of 0.8 m, housing three identical cylindrical floaters characterized by $R/d = 0.5$, $d_t/R = 0.25$, and $9R$ inter-body separation.

The validation process for the submerged structure is conducted in accordance with the numerical framework established by Rijnsdorp et al. [1] and Sergiienko et al. [60]. Employing identical parametric configurations to those

specified by Sergiienko et al. [60] – specifically $m = 268\,\text{t}$, $R = 5.5\,\text{m}$, $d_s = 3.75\,\text{m}$, $d_t = 5.5\,\text{m}$, and $h = 50\,\text{m}$ – a comparative analysis of the RAO is performed, as illustrated in Fig. 6. Given that the present investigation adopts the motion equation, PTO system, and mooring constraint formulations delineated by Sergiienko et al. [60], the computed RAO exhibits congruence under the operational parameters $B_{\text{pto}} = 10^5\,\text{N/(m/s)}$, $K_{\text{pto}} = 10^5\,\text{N/m}$, $\alpha_v = 44°$, and $l_0 = 56.6\,\text{m}$. Furthermore, utilizing the displacement constraints prescribed by Sergiienko et al. [14], where displacements in the surge and heave degrees of freedom are constrained by $s_{1,\text{max}} = \pi R/4 = 4.32\,\text{m}$ and $s_{3,\text{max}} = R/2 = 2.75\,\text{m}$ respectively, with regular wave height $H = 2\,\text{m}$, an evaluation of wave energy absorption performance is undertaken for three configurations: (a) floating ($z_n = 0$), (b) submerged ($z_n = 3.75\,\text{m}$), and (c) submerged ($z_n = 6.5\,\text{m}$), as depicted in Fig. 7. The computational outcomes demonstrate that the present results exhibit complete concordance with the numerical simulations reported by Sergiienko et al. [14, 60].

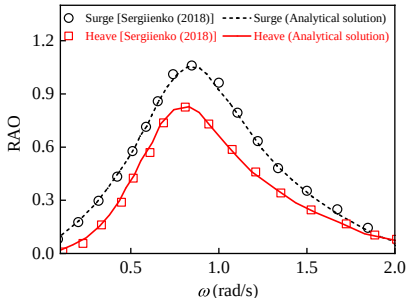

Fig. 6. Comparison of the motion response of submerged WEC in surge and heave mode at $m = 268$ t, $R = 5.5$ m, $d_s = 3.75$ m, $d_t = 5.5$ m, $h = 50$ m, $B_{pto} = 10^5$ N/(m/s), $K_{pto} = 10^5$ N/m, $\alpha_v = 44$ deg, $l_0 = 56.6$ m (Line: present analytical solution; dots: Sergiienko et al. [60]).

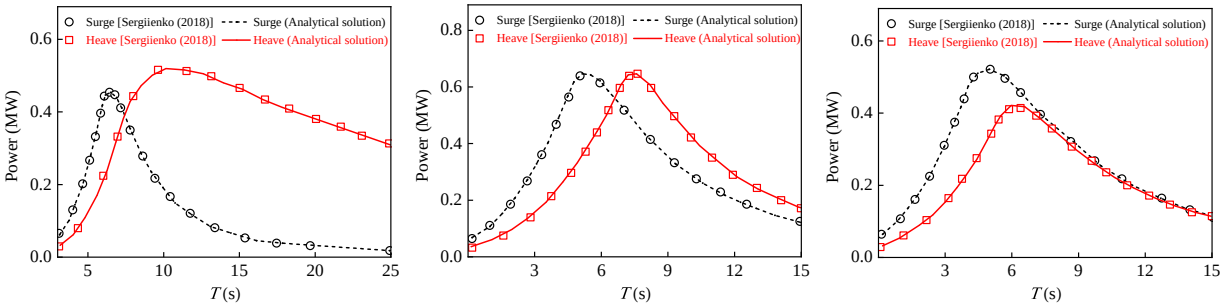

(a) $z_n = 0$ **(b)** $z_n = 3.75\,\text{m}$ **(c)** $z_n = 6.5\,\text{m}$

Fig. 7. Comparison of the wave power absorbed by FB and CETO devices in surge and heave modes with different submergence depth: (a) FB $z_n = 0$, (b) CETO $z_n = 3.75$ m, (c) CETO z_n=6.5 m (Line: present analytical solution; dots: Sergiienko et al. [14]).

Although comprehensive investigations of CETO arrays remain absent in extant literature, comparative assessments may be derived through validated numerical models. This study employs the computational model developed by Zhu et al. [23] (termed the AMA-system) for comparative analysis. Considering the potential degradation in numerical precision associated with boundary element method-based models during multi-body computations as float quantity increases [79, 80], an array configuration with $N = 9$ units is selected for analysis, as the computational fidelity of the AMA-system has been rigorously validated for arrays of similar scale [23]. In Fig. 8, the motion responses of the floating ($z_n = 0$) and submerged ($z_n = 5$) WECs, located at the midpoint of the last row of the array in the direction of wave propagation, are compared. The analysis employs $h/R = 10$, $R = d_t$, with mooring configurations, PTO damping coefficients, and stiffness coefficients adopted from Sergiienko et al. [60]. As evidenced in Fig. 8, the analytical solutions presented demonstrate remarkable congruence with AMA-system numerical predictions. Furthermore, in accordance with the theoretical framework delineated by Zhu et al. [49], the demonstrated precision of the current mathematical model in resolving hydrodynamic, kinematic, and energetic responses for reduced-scale arrays suggests its robust applicability to large-scale multi-body configurations. This computational capability is ex-

emplified in Zhu et al. [8], where analogous mathematical models enable accurate calculation of the fluid-structure interactions and kinematic behaviors for intricate buoy systems comprising N=84 units. These collective findings affirm the analytical validity and robustness of the proposed computational model.

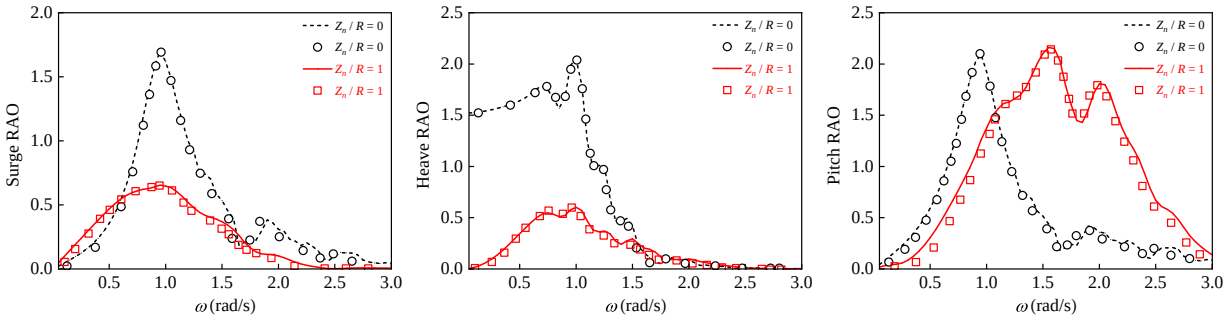

(a) surge mode **(b)** heave mode **(c)** pitch mode

Fig. 8. Comparison of motion RAO in the surge, heave, and pitch modes at $h/R = 10$, $R = d_t$ (Line: present analytical solution; dots: AMA-system Zhu et al. [23]).

4. Results and discussions

This section investigates the wave energy capture and hydrodynamic performance of the CETO system through the application of the analytical framework developed in this study. Given the limited multiparametric investigations on CETO systems, Section 4.1 conducts a comprehensive sensitivity analysis of operational parameters under realistic marine conditions and explores potential system optimization. Case studies clearly reveal the effects of PTO damping, stiffness, geometric dimensions, and submergence depth on the wave energy capture efficiency, bandwidth, and peak frequency in CETO system. Building on these insights, Section 4.2 conducts a pioneering comparative analysis of array-based FB and CETO systems, evaluating four critical aspects: (i) inter-unit hydrodynamic shadow effect, (ii) holistic energy harvesting efficacy across both integrated arrays and discrete units, (iii) kinematic stability metrics, (iv) wave surface characteristics for distinct FB and CETO layouts. The research findings indicate that the array-based configuration redefines the characteristics of the CETO and FB systems, highlighting the potential for the engineering application of the CETO system.

4.1. Multi-parameter study

4.1.1. Effect of PTO damping and stiffness

Although prior studies have investigated the effects of structural stiffness and damping on energy-harvesting optimization in standalone CETO systems, notable gaps remain concerning their influence on spectral energy capture characteristics—particularly peak magnitude, resonant frequency, and bandwidth. Furthermore, within the context of the CETO system, PTO damping and stiffness parameters exhibit significant coupling effects with the mooring dynamics, fundamentally governing the overall hydrodynamic response of the WEC. Therefore, the PTO damping and stiffness of the CETO system will be investigated initially. The geometric parameters, mooring system, and PTO type used here are based on the parameters in Section 3 (i.e., adopted by Sergiienko et al. [60]). Specifically, under fixed geometric conditions ($R/h = 0.11$, $d_s/h = 0.075$, $d_t/R = 1$) and zero PTO stiffness ($K_{\text{pto}} = 0$), the analysis focuses on quantifying the effects of PTO damping (B_{pto}). To facilitate generalized interpretation, non-dimensionalized parameters are introduced: $\overline{B}_{pto} = B_{pto}/(\rho g^{0.5} R^{2.5})$ and $\overline{K}_{pto} = K_{pto}/(\rho g R^2)$, enabling evaluation across varying operational conditions.

In Fig. 9a, the relationship between the q factor as a function of $\overline{B}_{pto}$ and the incident wave angular frequency ω is compared. As a whole, the frequency band of the q factor is mainly concentrated in the range of 0.5 to 2 rad/s, and the frequency of the spectral peak remains largely unaffected by $\overline{B}_{pto}$ ($\omega_r = 1.1$ rad/s). As $\overline{B}_{pto}$ gradually increases from 0, the q factor initially rises and then decreases, indicating the existence of an optimal point at $\overline{B}_{pto} = 6$, where

the q factor reaches the maximum. When $\overline{B}_{pto} \geq 20$, $q \leq 0.3$, signifying minimal oscillation of the CETO system. In Fig. 9b, a direct comparison of the variation of q with ω is presented, where the values of $\overline{B}_{pto}$ correspond to the reference lines in Fig. 9a. It is evident that within the range of $\overline{B}_{pto} = 4$ to 10, the q factor exhibits slight variations with $\overline{B}_{pto}$, with the q-curve attaining the largest peak and the widest bandwidth at $\overline{B}_{pto} = 6$. Additionally, according to the findings of Falnes [72]:

$$P_w = \frac{(B_{pto}/2)\,|F_D|^2}{[B_{pto} + B(\omega)]^2 + [\omega M_m + \omega A(\omega) - S_m/\omega]^2}, \tag{38}$$

where F_D is excitation wave force given by Eqs. 26 - 28; S_m is system stiffness (including the PTO, mooring system, and restoring stiffness). We note that $P_w = 0$ for $B_{pto} = 0$ and ∞, and that $P_w > 0$ for $0 < B_{pto} < \infty$. Thus, the maximum absorbed power occurs when $\partial P_w/\partial B_{pto} = 0$, which occurs if $B_{pto} = B(\omega)^2 + (\omega M_m + \omega A(\omega) - S_m/\omega)^2)$,

$$P_{w,\max} = \frac{|F_D|^2\,/4}{B(\omega) + \sqrt{B(\omega)^2 + \left[\omega M_m + \omega A(\omega) - S_m/\omega\right]^2}}. \tag{39}$$

According to the research by Sergiienko et al. [14], it was found that, compared to single-mode energy capture, multi-mode energy capture in the FB and CETO systems can capture more wave energy. Therefore, this study is based on a three-point mooring system, designed to capture wave energy from multiple modes. In the process of multi-mode analysis based on Eqs. 38 and 39, each mode corresponds to different $A(\omega)$ and $B(\omega)$, which in turn correspond to different B_{pto}. Thus, this study employs a parameter scanning method for optimization and reveals the effect of energy capture with the variation of PTO damping and stiffness [14, 60]. In addition, we observe from inspection of Eq. 38 that if we, for arbitrary B_{pto}, can choose $B(\omega)$ and S_m such that:

$$\omega[B(\omega) + B_{pto}] - S_m/\omega = 0. \tag{40}$$

then the absorbed power has the maximum value $P_w = |F_D|^2\,/(8B_{pto})$. However, at this parameter configuration, the PTO stiffness coefficient nullifies ($\overline{K}_{pto}$=0) and the system fails to achieve forced resonance conditions (as defined by Eq. 40), yielding a peak quality factor of merely $q = 0.47$. To enhance the wave energy capture by CETO, the parameter scanning method is employed to investigate the PTO stiffness and examine the effect of the variation of $\overline{K}_{pto}$ on the energy capture performance, as shown in Fig. 10. It can be observed that as $\overline{K}_{pto}$ increases, the peak frequency of the q factor increases slightly, while the peak value first increases and then decreases (see Fig. 10a). The bandwidth ω_0 is primarily concentrated between 0.5 and 2 rad/s. Specifically, when $\overline{K}_{pto} = 1$, the peak frequency $\omega_r = 1.05$ rad/s, and as $\overline{K}_{pto}$ increases to 25, ω_r increases to 1.4 rad/s. When $\overline{K}_{pto}$ is in the range of 3 to 8, the peak value of the q factor remains relatively high (i.e., $q \geq 0.68$). Figure 10b provides a more direct comparison of the variation in the q factor with the incident wave angular frequency. It is apparent that as $\overline{K}_{pto}$ increases, the bandwidth slightly narrows. When $\overline{K}_{pto} = 1$, $\omega_0 \in [0.25, 2.3]$ rad/s, and when $\overline{K}_{pto} = 25$, $\omega_0 \in [0.65, 2.3]$ rad/s, indicating a reduction in energy capture within the low-frequency range. Furthermore, it is observed that when $\overline{K}_{pto} > 10$, as PTO stiffness continues to increase, the peak value of the q-curve decreases sharply, which is mainly manifested in the constraints on the motion response of the system.

4.1.2. Effect of geometric dimensions and submersion depth

With respect to the CETO structure, the geometric parameters primarily encompass the radius and thickness of the body. Initially, under the condition $R/d_t = 1$ and $d_s/h = 0.075$, the motion response as function of radius R and angular frequency ω is compared for the undamped and stiffness-free condition, as well as for the optimal damping and stiffness condition, as illustrated in Fig. 11. In surge mode (refer to Figs. 11a and 11d), the bandwidth of motion RAO under undamped and stiffness-free condition predominantly lies within the range $0.1 < \omega_0 < 2.2$ rad/s, with the spectral peak frequency remaining stable at $\omega_r = 0.24$ rad/s as R increases. By contrast, under optimal damping and stiffness conditions, the surge RAO bandwidth is concentrated in the region of $0.4 < \omega_0 < 2.6$ rad/s. As the radius R increases, the peak frequency gradually decreases, while the surge RAO increases progressively. In heave mode (refer to Figs. 11b and 11e), the performance of bandwidth and peak frequency are similar to those observed in the

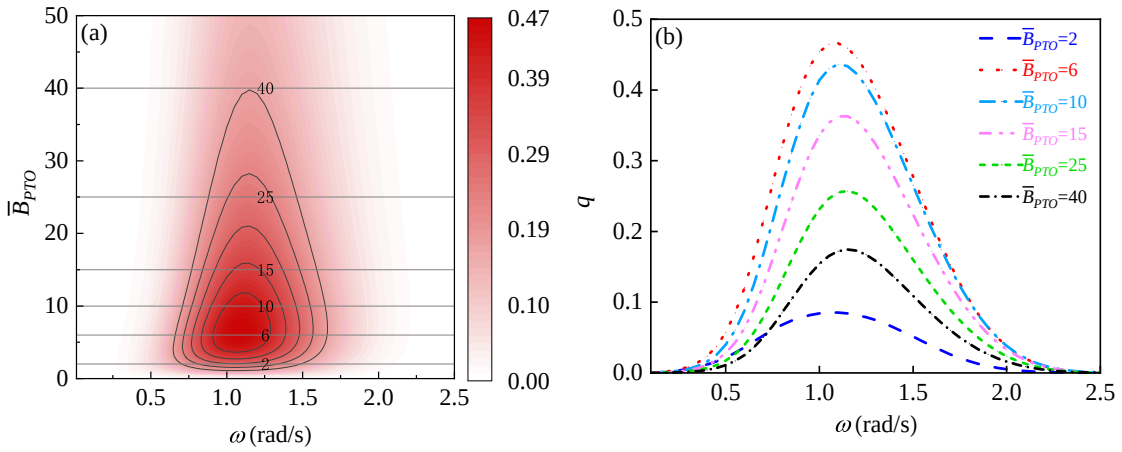

Fig. 9. Effect of PTO damping coefficients $\overline{B}_{pto}$ on wave energy capture q factor at stiffness coefficient $\overline{K}_{pto} = 0$, $R/h = 0.11$, $d_s/h = 0.075$, $d_t/R = 1$ [60].

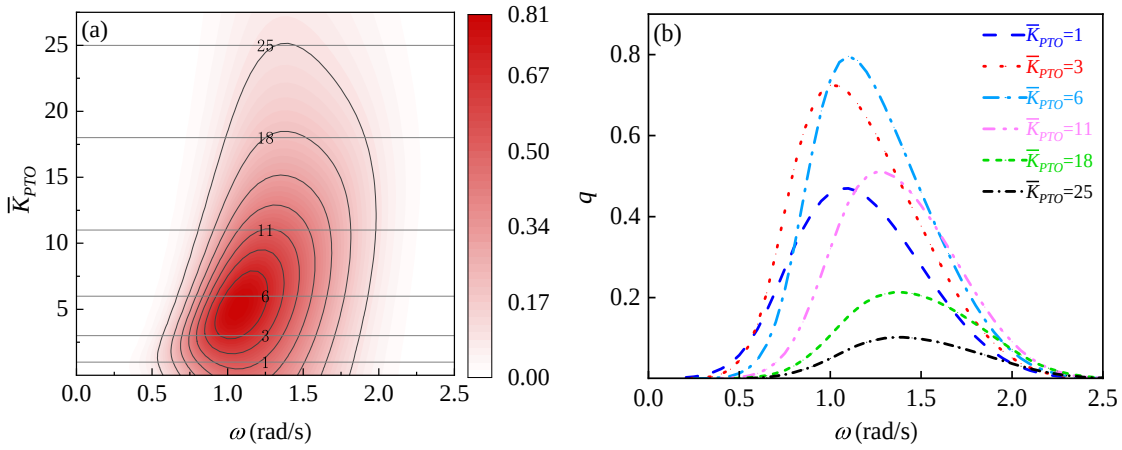

Fig. 10. Effect of stiffness coefficients $\overline{K}_{pto}$ on wave energy capture q factor at $\overline{B}_{pto} = 6$, R/h=0.11, $d_s/h = 0.075$, $d_t/R = 1$ [60].

surge mode. The main difference is that, in the undamped, stiffness-free case, the heave RAO at the peak frequency decreases markedly as R increases. In contrast, under optimal damping and stiffness conditions, the heave RAO at the peak frequency initially increases and then decreases as R increases, although the variation is relatively small (i.e., when R/A =1, 5 and 10, the maximum motion RAO are 0.51, 0.72, and 0.63, respectively). In the pitch mode (refer to Figs. 11c and 11f), the region of bandwidth for the undamped and stiffness-free condition is primarily concentrated in $\omega_0 \in [0.1, 3.4]$ rad/s, with the peak amplitude gradually decreasing as R increases. With optimal damping and stiffness, the pitch RAO is mainly confined to $\omega_0 \in [0.8, 3.4]$ rad/s, which serves to attenuate the low-frequency motion response in comparison to the undamped and stiffness-free configuration. As R increases, the peak amplitude undergoes a substantial reduction (i.e., when $R/A > 5$, the peak amplitude drops below 1.5°).

Overall, as R increases, the bandwidth of the motion RAO narrows significantly, regardless of the damping and stiffness modes. Specifically, under the optimal damping and stiffness condition, the peak frequencies and bandwidths region of the RAO-curves in the surge and heave modes shift to the left as R increases, while the RAO values decrease substantially with the assignment of damping and stiffness in three modes. This can be attributed to two factors: first, as the radius increases, the characteristic length of the structure becomes larger than the wavelength, reducing

sensitivity to short-period waves and thereby decreasing the motion response in the high-frequency region. Second, according to the equation $\omega_r = \sqrt{\frac{S_m}{M_m+A(\omega)}}$, as R and M_m increase, the resonance frequency ω_r is reduced that makes the RAO-curve shift to the left. Moreover, as illustrated in Fig. 11, damping and stiffness significantly influence the spectral peak frequency, operational bandwidth, and peak magnitude of the motion. Consequently, to achieve meaningful optimization outcomes, both damping and stiffness parameters must be systematically incorporated into the multiparametric design optimization framework of the CETO system.

Under the optimal damping and stiffness condition, the relationship between the q-factor and ω for different radii is studied, as shown in Fig. 12. It is clearly evident that as R increases, both the spectral peak frequency and bandwidth of the q-curve shift towards lower frequencies, while the peak value increases significantly. Specifically, when R/A increases from 1 to 10, ω_r decreases from 1.7 to 0.77 rad/s, the bandwidth changes from $\omega_0 \in [0.6, 2.8]$ rad/s to $\omega_0 \in [0.3, 1.7]$ rad/s, and the peak value increases from 0.1 to 1.05. This is primarily because when R/A decreases, the submergence depth d_s of the floats remains unchanged, resulting in a significantly reduced motion response for smaller full-submerged buoys under deeper submersion conditions, thereby suppressing wave energy capture. Furthermore, Fig. 12 further illustrates that the CETO system exhibits varying energy capture characteristics across different incident wave frequency ranges, highlighting the necessity of studying the system within the context of specific sea states.

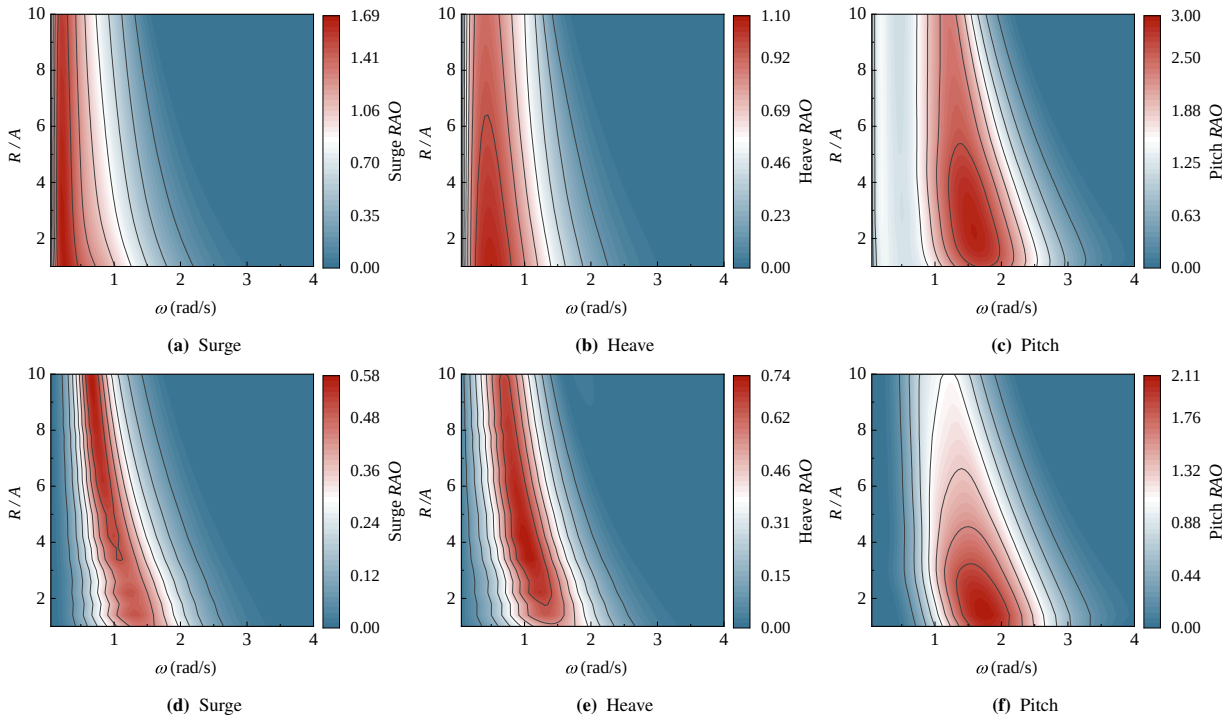

Fig. 11. Contour plots for the variation of CETO motion RAO as a function of the angle frequency ω and WEC radius R at $R/d_t = 1$, $d_s/h = 0.075$: (a), (b) and (c) with $\overline{K}_{pto} = 0$ and $\overline{B}_{pto} = 0$; (d), (e) and (f) with optimal damping and stiffness coefficients.

To this end, the investigation will focus on the marine environment surrounding Zhaitang Island, Qingdao, China (35°36.2′ N, 119°56.15′ E) (Fig. 13), aiming to investigate and optimize the energy capture performance of the CETO system. Data were recorded using a Nortek AWAC-ADCP with a sampling interval of 1 hour and a sampling frequency of 2 Hz (data for June and December were missing due to instrument malfunction). In Fig. 14a, a total of 10 months of data are selected, with red representing the average period T_a of the wave and blue representing the significant wave height H_s. Figure 14b shows the joint probability distribution of the significant wave height and the wave peak periods T_p, with the probability expressed as a percentage. The corresponding annual wave energy is presented in Fig. 14c. H_s predominantly falls within the range of 0.3 m to 0.8 m, while T_p is mainly distributed

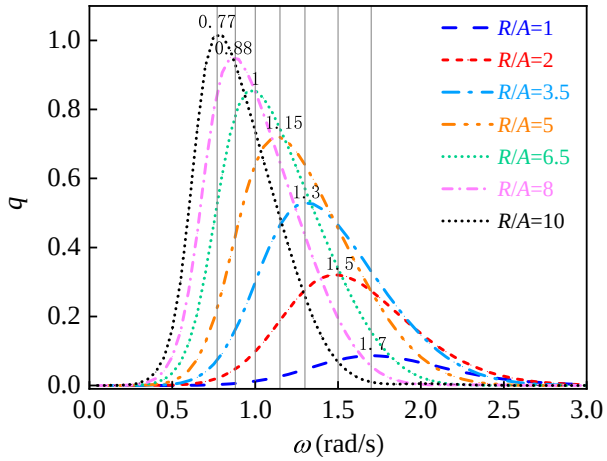

Fig. 12. Comparison of the effect of seven different CETO radii R on wave energy capture performance at $R/d_t = 1$ and $d_s/h = 0.075$.

between 3 s and 5 s. The annual average significant wave height is approximately 0.6 m, and the wave peak period is around 4.2 s. A scaled wave spectrum is employed in this study. Based on the wave conditions at Zhaitang Island and the relationship between the q, ω and R, the value of $R/A = 5$ is selected for the following case study. Additionally, the PTO damping and stiffness are selected as optimal values based on the parametric scanning method with the q factor as the objective function, as in the aforementioned subsection [14].

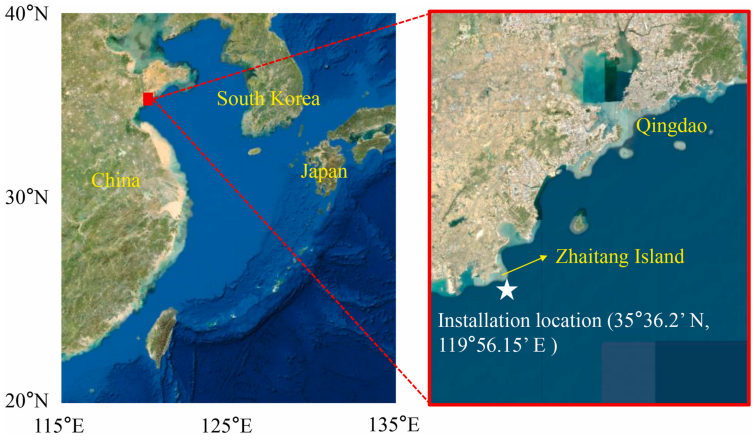

Fig. 13. The map of the installation located in the sea area of Zhaitang Island at 35°36.2′ N, 119°56.15′ E [81].

In Fig. 15, the motion RAO and wave energy capture efficiency of CETO as a function of the float thickness d_t/R and ω is investigated at $d_s/R = 0.2$, 0.4, 0.6, 0.8 and 1, respectively. In surge mode (Figs. 15a~15e), the peak surge RAO magnitude exhibits positive correlation with both structural thickness and submergence depth, whereas the float's motion response in the frequency domain $\omega \in [2, 3]$ rad/s demonstrates inverse proportionality to increasing d_t. In particular, as the thickness increases, the primary bandwidth of the surge RAO remains essentially unchanged, concentrating in $\omega_0 \in [0.3, 1.7]$ rad/s, with the corresponding peak frequency gradually decreasing (e.g., when $d_t/R = 0.1$ and 2, the peak frequencies are 1.5 and 0.7 rad/s, respectively). In the heave mode (see Figs. 15f ~ 15j), as the submersion depth d_t increases, the heave RAO shows a decreasing trend, particularly in the primary bandwidth $\omega_0 \in [0.1, 2]$ rad/s and the high-frequency region $\omega \in [2, 3]$ rad/s. As the radius d_t increases, the peak values within the primary bandwidth initially rise before subsequently declining, while the bandwidth and peak frequency remain constant, predominantly concentrated in the range $\omega_0 \in [0.1, 2]$ rad/s and $\omega_r = 0.9$ rad/s. Furthermore, for different submersion depths, there exists a specific value of d_t that maximizes the heave RAO, and this value (denoted as $d_{t,\max}$)

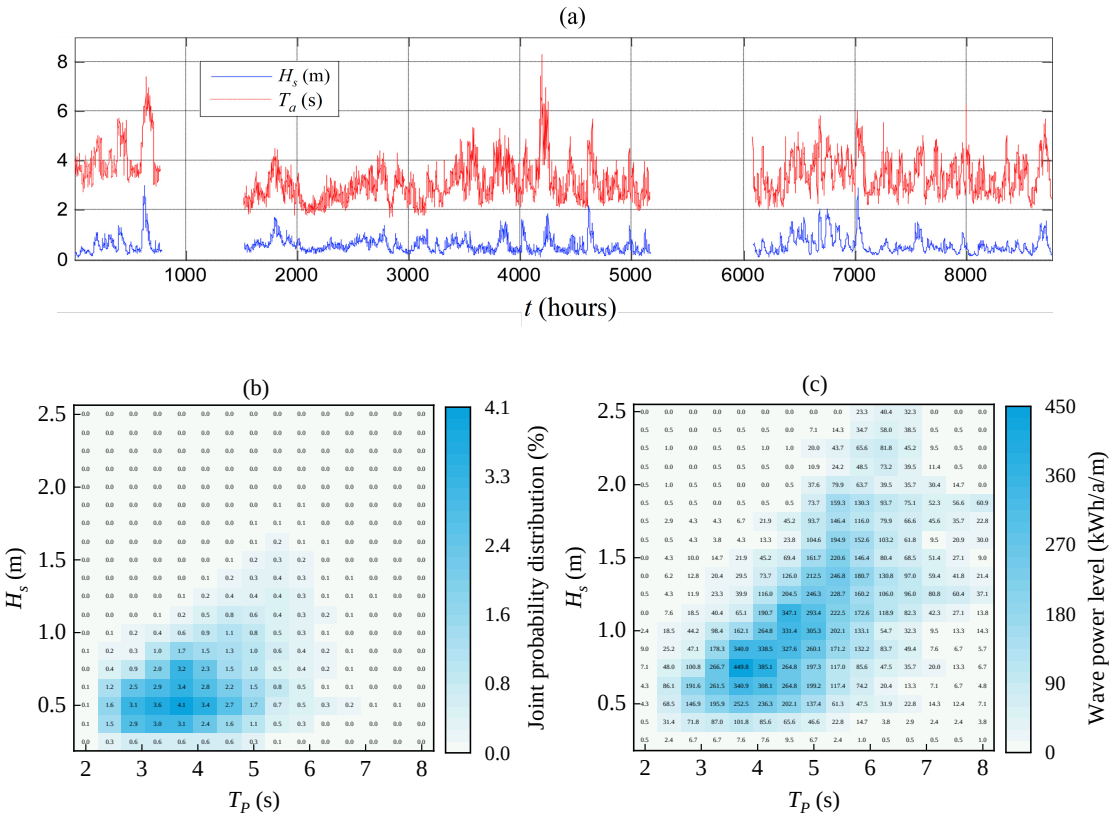

Fig. 14. Measured data for the south-eastern part of Zhaitang Island: (a) 10 months of wave data where the blue line represents significant wave heights and the red line represents the average wave period; (b) scatter diagram of wave data statistics; and (c) scatter diagram of wave energy distribution.

decreases as the submersion depth increases. For instance, when $d_t/R = 0.2$, $d_{t,\max}/R = 0.9$, and when $d_t/R = 1$, $d_{t,\max}/R = 0.5$. In the pitch mode (see Figs. 15k ~ 15o), the pitch RAO exhibits a significant reduction with increasing d_t. This phenomenon is principally governed by the augmented submergence depth, which reduces the magnitude of hydrodynamic excitation forces acting on the submerged structure, while the radiation-induced additional mass and damping coefficients exhibit minimal variations within the frequency spectrum. As the thickness d_t increases, the pitch RAO exhibits a slight initial increase followed by a significant decrease, with the bandwidth and peak frequency remaining virtually unchanged, concentrated in $\omega_0 \in [0.5, 2.9]$ rad/s and $\omega_r = 1.5$ rad/s.

Following Sergiienko et al. [14, 60], when the incident wave propagates along $\beta = 0$, the CETO primarily exhibits motion in surge, heave, and pitch degrees of freedom. The wave energy is mainly captured through the surge and heave modes, and therefore, the motion response characteristics of these two modes jointly determine the performance of the captured wave power, as shown in Figs. 15p ~ 15t. The analysis reveals two key trends: as the thickness d_t/R increases from 0 to 2, the q factor initially ascends and subsequently stabilizes in the region of $0.5 < \omega < 2$ rad/s. Furthermore, while increasing the submersion depth d_t exhibits a relatively minor influence on the bandwidth and peak frequency of the q factor, it significantly attenuates the q factor magnitude across the operational spectrum. Based on these observations, $d_t/R = 1$ is recommended for subsequent studies (Fig. 15), as this ratio ensures stable maximum q factor values within the primary dynamic response bandwidth while maximizing motion stability across all three modes—consistent with the R/d_t ratios validated in Sergiienko et al. [14, 60].

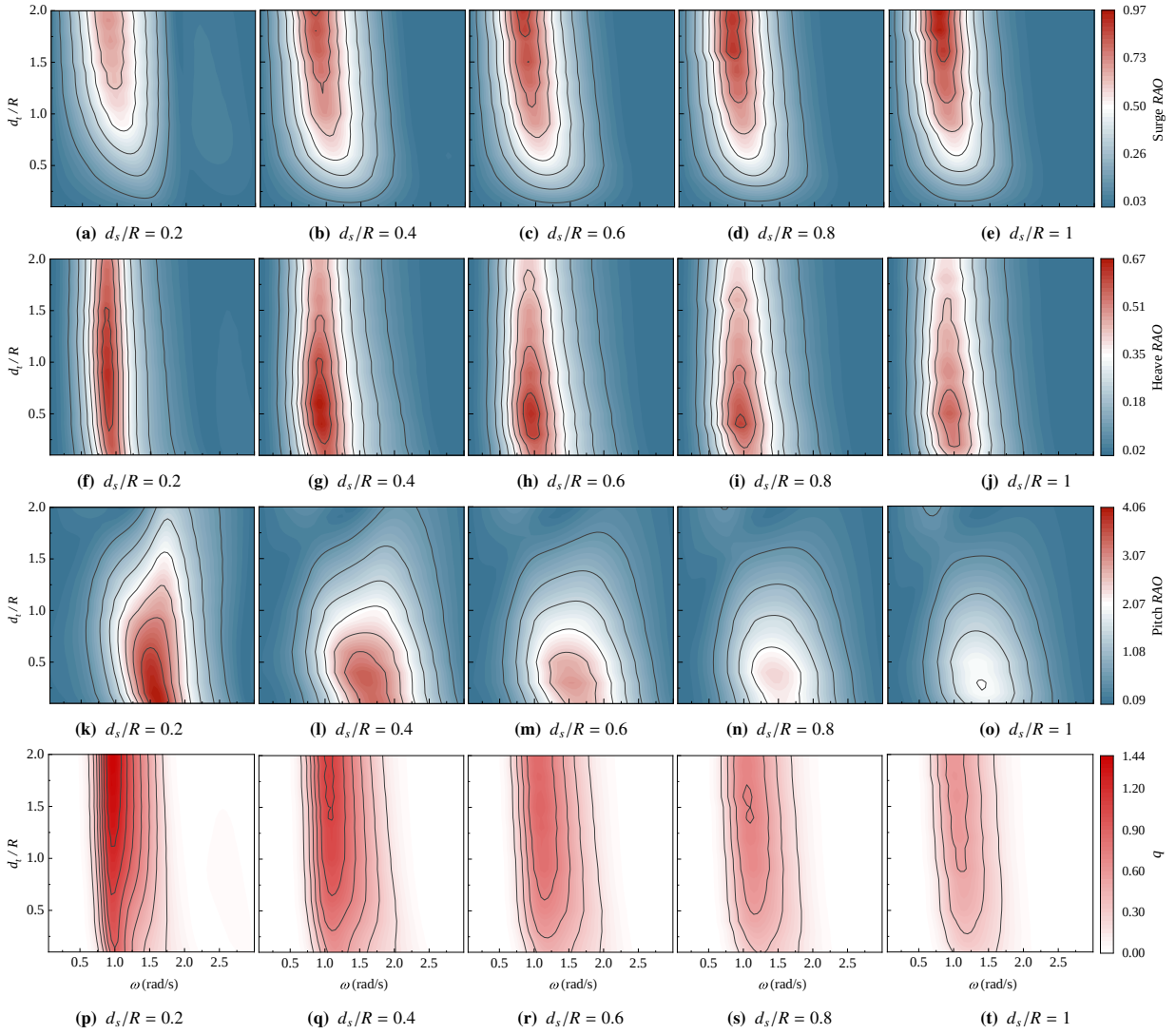

Fig. 15. Contour plots for the motion response of CETO in (a)~(o) and wave energy capture performance in (p)~(t) as function of wave angle frequency ω and dimensionless thickness d_t/R, in which the first column (a), (f), (k) and (p) with $d_s/R = 0.2$; the second column (b), (g), (l) and (q) with $d_s/R = 0.4$, the third column (c), (h), (m) and (r) with $d_s/R = 0.6$, the fourth column (d), (i), (n) and (s) with $d_s/R = 0.8$; and the fifth column (e), (j), (o) and (t) with $d_s/R = 1$.

4.2. Study on array-based systems

4.2.1. Effect of shadow and layout

To examine the energy capture characteristics of array-based versus standalone systems, Fig. 16 illustrates the energy capture performance of a standalone WEC, encompassing both FB (with $z_n/R = 0$) and CETO (with $z_n/R > 0$). The selection of WEC parameters follows the results of the previous section, adopting $R/d_t = 1$, $h/R = 10$, and the same methodology for PTO damping and stiffness [14, 60]. As depicted in Fig. 16, for standalone systems, increasing the submersion depth leads to a significant reduction in both the peak value and the bandwidth of the q-curve. Furthermore, for both FB and CETO at varying submersion depths, the peak frequency of the q-curve remains around 1.0 rad/s. When $z_n/R = 0 \sim 1.0$, the bandwidth is concentrated within the range of 0.5 to 2.5 rad/s. However, as the submersion depth increases further—specifically for $z_n/R = 1.5 \sim 2$—the bandwidth contracts to $0.5 \sim 1.9$ rad/s, signifying a diminished energy capture in the high-frequency region. This constraint presents challenges for energy extraction in specific coastal areas, such as the Zhaitang Island region. Therefore, it can be inferred that FB

demonstrates superior energy capture performance compared to CETO in the standalone system. However, the energy capture characteristics of array-based CETO systems remain largely unexplored. To bridge this research gap, the present study will conduct a comprehensive analysis of the energy capture performance of CETO array-based systems and provide a comparative evaluation against the FB system.

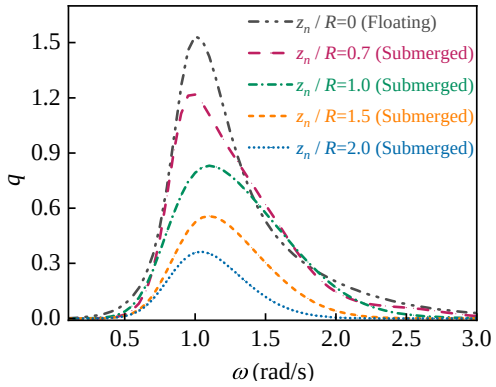

Fig. 16. Comparison of the effect of five different submergence depth z_n/R on wave energy capture performance of standalone WECs at $R/d_t = 1$ and $h/R = 10$.

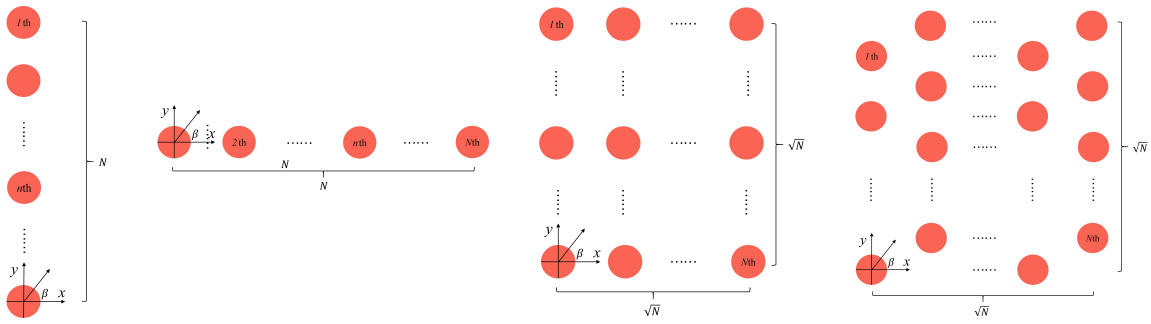

Fig. 17. Four distinct arrangements of N WECs with equal center-to-center spacing d_w between adjacent floats.

For this purpose, the wave energy capture performance of four array configurations is analyzed to examine the shadow effect observed in wave-structure interactions. As illustrated in Fig. 17, the four arrays are designated as #1, #2, #3, and #4, each comprising 25 identical WECs (i.e., $N = 25$), with a center-to-center spacing of $d_w = 20R$ between adjacent floats [14]. Figure 18 illustrates the spectral characteristics of the q factor for the nth WEC at angular frequency ω, denoted as $Q_n(\omega)$ in arrays #1 and #2. Figures 18a to 18d illustrate the energy capture performance for #1 array at immersion depths of $z_n/R = 0$, 0.7, 1.0, and 1.5, respectively. It is observed that as n increases, the peak frequency of $q_n(\omega)$ remains largely unchanged, while its peak magnitude declines significantly. Specifically, for structures with $z_n/R = 0$ and 0.7, both bandwidth and peak value of $q_n(\omega)$ exhibit a substantial decrease with increasing n, demonstrating pronounced shadow effect. In contrast, for structures with $z_n/R = 1$ and 1.5, although the peak value of $q_n(\omega)$ gradually diminishes with increasing n, the rate of decline is slower compared to those with $z_n/R = 0$ and 0.7, and the bandwidth expands slightly. Therefore, in the #1 configuration, while significant shadow effect are observed for both the FB and CETO systems, the intensity of the shadow effect diminishes as submersion depth increases. Moreover, interactions among multiple floats may further broaden the bandwidth for CETO wave energy capture.

In Figs. 18e to 18h, the wave energy capture performance of array #2 under four different submersion depths is examined. It is evident that when the array is aligned perpendicular to the incident wave direction, the $q_n(\omega)$ of any WEC in the array remains nearly identical, indicating the absence of a shadow effect. Furthermore, due to diffraction

and radiation interactions among multiple floats, the motion responses of adjacent systems are further amplified, thereby enhancing wave energy capture. Although this array gain phenomenon for FB WECs in array #2 has been extensively discussed in prior studies [23, 74], similar effects are also observed in the CETO systems.

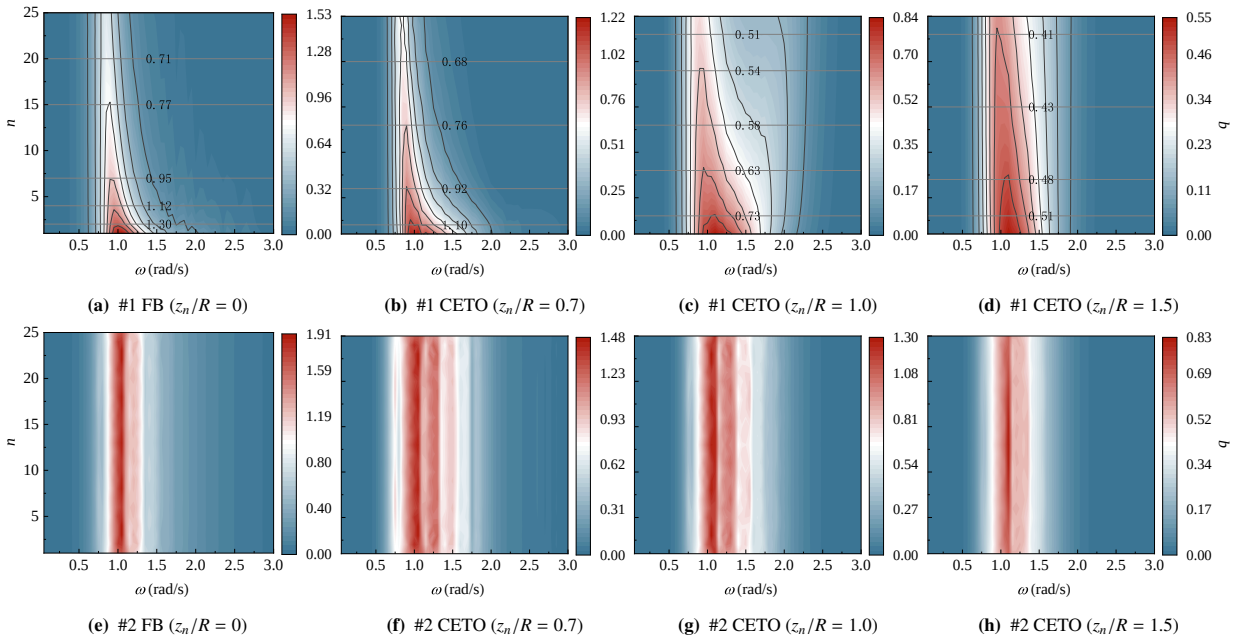

(a) #1 FB ($z_n/R = 0$) **(b)** #1 CETO ($z_n/R = 0.7$) **(c)** #1 CETO ($z_n/R = 1.0$) **(d)** #1 CETO ($z_n/R = 1.5$)

(e) #2 FB ($z_n/R = 0$) **(f)** #2 CETO ($z_n/R = 0.7$) **(g)** #2 CETO ($z_n/R = 1.0$) **(h)** #2 CETO ($z_n/R = 1.5$)

Fig. 18. Wave energy capture factor of the nth WEC, $q_n(\omega)$, under #1 and #2 configurations as a function of wave frequency ω.

Since the $q_n(\omega)$ of #3 and #4 arrays does not exhibit a continuously varying pattern as n increases as for the #1 and #2 arrays, the energy capture characteristics of #3 and #4 are investigated using the format presented in Fig. 19. The horizontal and vertical axes correspond to the x and y coordinates of the WECs, respectively, with each grid representing the average $q_n(\omega)$ of the nth WEC over the frequency range $\omega \in [0, 3]$ rad/s, defined as $\overline{q}_n$. Figures 19a to 19d illustrate the energy capture characteristics of #3 array for $z_n/R = 0$, 0.7, 1.0, and 1.5. It is evident that as the submersion depth increases, the shadow effect diminishes significantly. This leads to a more uniform energy contribution from each unit, effectively mitigating extreme energy capture in individual units and enhancing structural resilience against wave-induced damage. The energy capture characteristics of #4 array for $z_n/R = 0$, 0.7, 1.0, and 1.5 are presented in Figs. 19e to 19h. It is observed that, in contrast to #3 array, the shadow effect does not decrease substantially as the submersion depth increases, and the wave energy capture distribution across the array remains uneven, leading to significantly higher energy capture in certain units while others exhibit lower utilization. This phenomenon may accelerate structural fatigue and reduce the operational lifespan of specific units.

To further investigate the energy capture characteristics of the four array configurations (i.e., #1 $\sim$ #4) under different submersion conditions ($z_n/R = 0$, 0.7, 1.0, and 1.5), frequency band area charts and violin plots are employed for analysis, as shown in Fig. 20. In the frequency band area charts (see Figs. 20a $\sim$ 20d), the vertical axis represents $\overline{q}_{array} = \frac{\sum_{n=1}^{N} q_n(\omega)}{N}$. It is evident that a significant disparity exists between the energy capture characteristics of array-based and standalone systems. In array-based systems, the FB system does not demonstrate superior energy capture performance; in some configurations, it even underperforms compared to the CETO system. For instance, in the #1 array, although the peak value of the $\overline{q}_{array}$-curve for the FB system is higher, both its bandwidth and band area are considerably smaller than those of the CETO array system at $z_n/R = 1.0$, and the CETO system has a wider bandwidth, making it more suitable for real sea states. Furthermore, Fig. 20 is primarily used to investigate shadow effect in FB and CETO arrays, configurations that are less likely to be adopted in practical engineering applications. Therefore, greater emphasis should be placed on arrays #3 and #4. In Fig. 20c, it can be observed that for $z_n/R = 0$, 0.7, and 1.0, the band areas are comparable, but the bandwidth of the CETO array is substantially larger than that of the FB array. Additionally, in contrast to the $\overline{q}_{array}$-curves for $z_n/R = 0$ and 0.7, the curve for $z_n/R = 1.0$ exhibits a lower peak value,

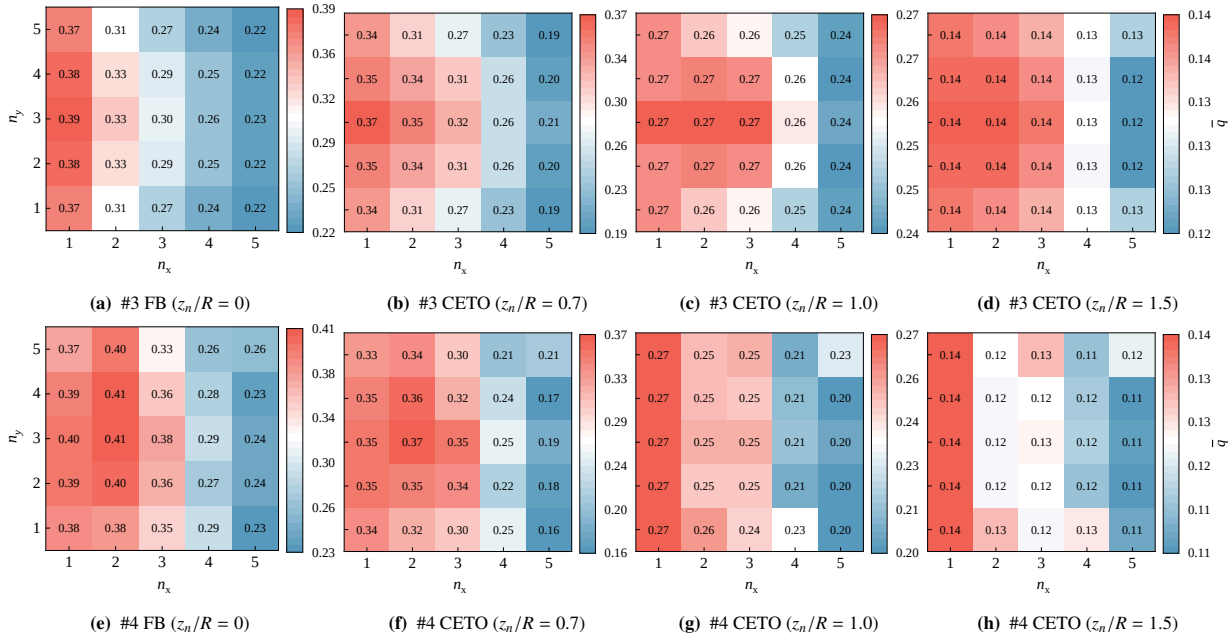

Fig. 19. Average wave energy capture factor $\overline{q}_n$ of nth WEC over the frequency range $\omega \in [0, 3]$ rad/s for #3 and #4 configurations.

with a more uniform energy distribution across the frequency band. This phenomenon has the potential to mitigate the risk of structural damage in engineering applications by alleviating the impact of severe wave conditions. In #4 array (see Fig. 20d), although the bandwidth is comparable to that of #3 array, the distribution exhibits greater irregularity. With the exception of the FB system, the band area of the CETO system is reduced relative to that of #3 array, particularly for the array at $z_n/R = 1$. Furthermore, as observed in Fig. 20, when $z_n/R = 1.5$, the band area, peak size, and bandwidth experience a notable decline, significantly limiting the wave energy capture capability. Figures 20e ~ 20h illustrate the $\overline{q}_{array}$ for each unit in the array over the frequency range $\omega \in [0.5, 2.5]$ rad/s at different submersion depths, providing a clear representation of the energy capture performance of each WEC in the array. In general, the energy distribution within the FB array is the most heterogeneous, followed by the CETO array at $z_n/R = 0.7$, whereas the CETO array at $z_n/R = 1$ exhibits the most uniform distribution among all four array configurations. For instance, in array #1, approximately 50% of the WECs in the FB array have a $\overline{q}_n$ factor below 0.2, whereas for the CETO array at $z_n/R = 1$, 50% of the units achieve a $\overline{q}_n$ exceeding 0.3. For the engineering-relevant configurations #3 and #4 (see Figs 20g and 20h), it can be seen that in the #3 array, the mean values for $z_n/R = 0$, 0.7 and 1 are approximately 0.3, while in the #4 array, the mean value for $z_n/R = 1$ is marginally below 0.3.

To rigorously elucidate the performance of arrays #3 and #4, statistical metrics are employed to enable a more comprehensive analysis, as illustrated in Fig. 21. Figures 21a, 21b, and 21c depict the maximum RAOs for the surge, heave, and pitch modes, respectively, across the frequency spectrum $\omega \in [0, 3]$ rad/s. In the surge mode, the maximum surge RAOs for the standalone and array-based systems are comparable; however, the CETO structure markedly attenuates the motion response in comparison to the FB structure. In heave mode, the normalized peak response $\overline{X}_{3,\max}$ remains analogous for draft ratios $z_n/R = 1$ and 1.5, whereas for $z_n/R = 0$ and 0.7, #3 array exhibits the highest heave motion response, followed by #4 array. Regarding pitch behavior, for $z_n/R = 0.7$, #4 array significantly amplifies the maximum pitch RAO $\overline{X}_{5,\max}$, while the $\overline{X}_{5,\max}$ values under other conditions remain relatively consistent. Nevertheless, the maximum pitch RAO does not exceed 5°, indicating that the system maintains considerable stability in the pitch mode. Thus, from the perspective of maximum motion RAO, the CETO system demonstrates significantly enhanced stability, while the performance of arrays #3 and #4 remains largely comparable.

The statistical values of wave energy capture for configurations #3 and #4 under four submersion depths are presented in Figs. 21d ~ 21e. Tailored to the hydrographic conditions of the Zhaitang Island maritime zone, Figs. 21d and 21e comparatively analyze spectral energy integration across frequency domains $\omega \in [0, 3]$ rad/s and $\omega \in [1, 3]$

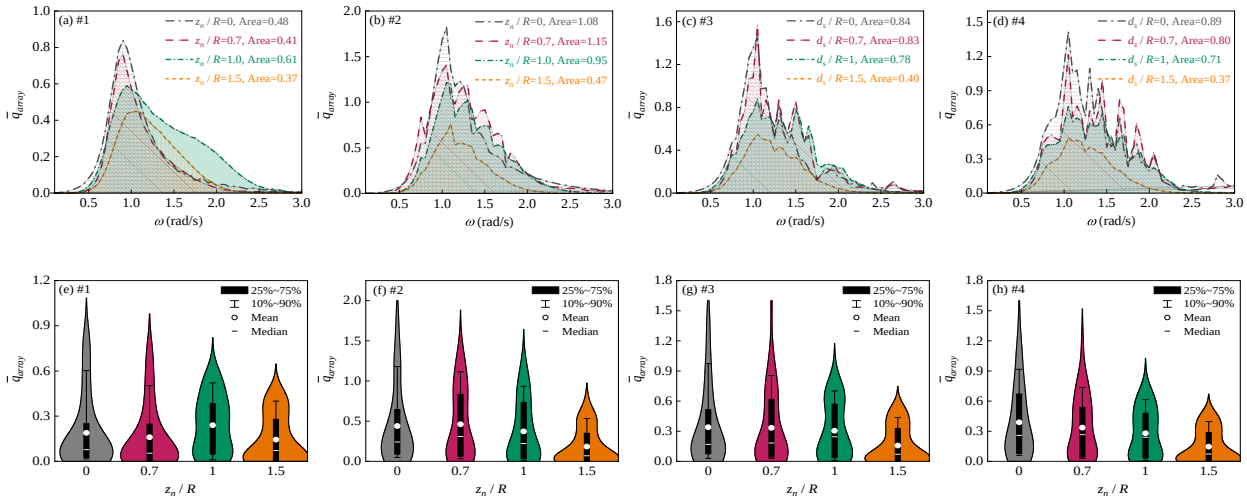

Fig. 20. Comparison of energy capture performance of the FB system ($z_n/R = 0$) and the CETO system ($z_n/R = 0.7, 1.0, 1.5$) under four different configurations (i.e., #1 ∼ #4). Figs. (a) to (d) show the band area comparison, while Figs. (e) to (h) present the violin plots in the frequency range $\omega \in [0, 3]$ rad/s.

rad/s, respectively, quantified through the metrics: $\overline{A}_{all} = \frac{\sum_{i=1}^{N}\int_0^3 q_n(\omega)d\omega}{N}$, $\overline{A}_{1-3} = \frac{\sum_{i=1}^{N}\int_1^3 q_n(\omega)d\omega}{N}$. Notably, at draft ratios $z_n/R = 1$ and 1.5, both the standalone WEC and #3 configuration exhibit marginally superior integration areas compared to #4. Conversely, for $z_n/R = 0$ and 0.7, the standalone WEC demonstrates significantly enhanced energy capture, particularly within the broader $\omega \in [0, 3]$ rad/s spectrum. Furthermore, at $z_n/R = 0$, configurations #3 and #4 demonstrate comparable efficacy in energy harvesting across $\omega \in [0, 3]$ rad/s, while #4 configuration outperforms #3 in the $\omega \in [1, 3]$ rad/s subdomain, aligning with the standalone system's performance. Under remaining operational conditions, both array configurations exhibit analogous energy capture characteristics. Figures 21f and 21g quantitatively contrast the mean ($\overline{q}_{mean}$) and standard deviation of energy flux density ($\overline{q}_{\text{Std.dev}}$) across $\omega \in [0, 3]$ rad/s (i.e., $\overline{q}_{mean} = \frac{1}{N}\sum_{i=1}^{N}\overline{q}_n$, $\overline{q}_{\text{Std.dev}} = \frac{1}{N}\sum_{i=1}^{N}(\overline{q}_n - \overline{q}_{mean})^2$). Fig. 21f reveals that at $z_n/R = 1$ and 1.5, $\overline{q}_{mean}$ values for the standalone WEC and #3 configuration are statistically congruent yet marginally exceed those of #4 configuration. Conversely, at $z_n/R = 0$ and 0.7, the standalone WEC achieves substantially higher $\overline{q}_{mean}$ relative to both configurations. Fig. 21g demonstrates that across all submersion depths, the standalone WEC exhibits superior energy flux consistency compared to #3 configuration, which in turn surpasses #4, particularly evident at $z_n/R = 0$ and 0.7.

An evaluation of wave energy capture performance, quantified through the metrics $\overline{q}_{\text{array}}$, $\overline{A}_{\text{all}}$, and $\overline{q}_{\text{mean}}$, reveals that the CETO and FB arrays at submersion depths $z_n/R = 0.7$ and 1 demonstrate comparable performance metrics (see Figs. 20a ∼ 20d and Figs. 21d ∼ 21g). For the FB and CETO arrays investigated, when $z_n/R = 1$, the energy-capture distribution among WEC units is most uniform, yielding the highest stability (see Fig. 19 and Figs. 20e ∼ 20h). Notably, while the $z_n/R = 1$ array exhibits spectral energy integration comparable to configurations at $z_n/R = 0$ and 0.7, it demonstrates reduced $\overline{q}_{\text{array}}$ magnitudes at resonance frequencies (e.g., $\omega \approx 1$ rad/s). This characteristic may mitigate wave-induced structural stresses during extreme hydrodynamic conditions (see Figs. 20g and 20h). Furthermore, the CETO system consistently outperforms the FB counterpart in motion stability across all operational modes (see Figs. 21a ∼ 21c). Given that the $z_n/R = 1$ array offers higher motion stability, lower shadow effect, more uniform wave energy capture distribution among WEC units, and comparable power capture, $z_n/R = 1$ is selected for further investigation of the performance of #3 and #4 configurations in subsequent studies.

To comprehensively evaluate the performance of #3 and #4 configurations, Fig. 22 juxtaposes the $\overline{q}_{mean}$ values for each WEC across frequency domains $\omega \in [0, 3]$ and $\omega \in [1, 3]$ rad/s, supplemented by the respective marginal and variance distributions. Scrutiny of $\overline{q}_{mean}$ magnitudes and marginal distributions reveals that #3 configuration exhibits superior wave energy conversion efficiency relative to #4 configuration. A comparative assessment of $\overline{q}_{\text{Std.dev}}$ demonstrates that the area of the $q_{Std.dev}$-curve follows the sequence: #3 ($\omega = 1 \sim 3$), #3 ($\omega = 0 \sim 3$), #4 ($\omega =$

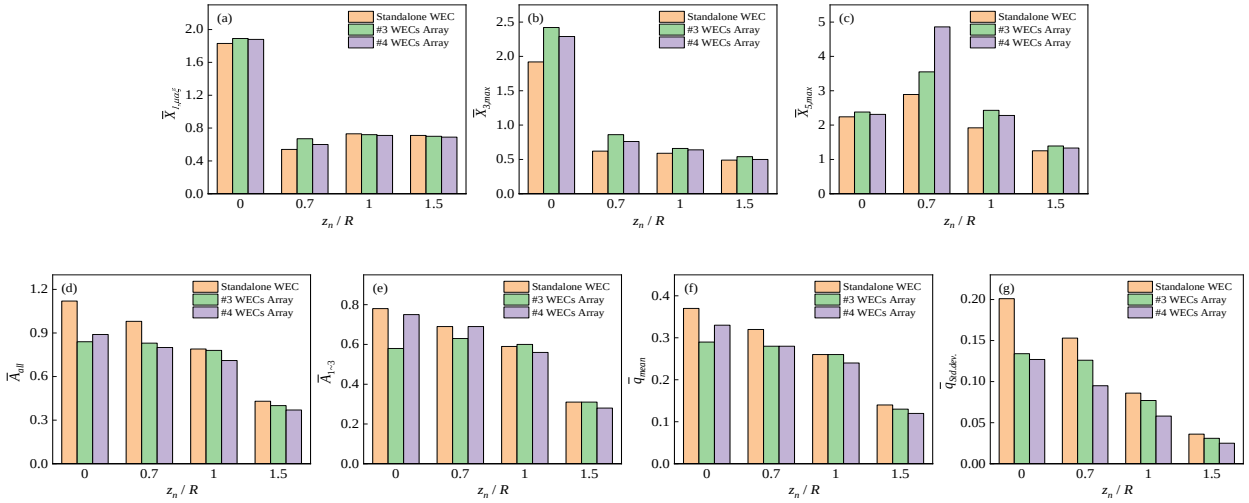

Fig. 21. Statistical comparison of standalone and array-based (configurations #3 and #4) WECs under four distinct submersion regimes: $z_n/R = 0$ (buoyant-body system) and $z_n/R = 0.7, 1.0, 1.5$ (submerged CETO-type systems).

$1 \sim 3$), and #4 ($\omega = 0 \sim 3$). This phenomenon predominantly stems from the elevated $\overline{q}_{mean}$ values observed in #3 configuration, which induces marginally amplified spectral deviations of $q_n(\omega)$ within the bandwidth. Furthermore, these discrepancies become increasingly conspicuous with ascending n, underscoring the progressive attenuation of energy harvesting efficacy in rear-row units due to hydrodynamic shadow effect. Notably, #4 array manifests pronounced $\overline{q}_{mean}$ diminution as n escalates, particularly for $n > 15$.

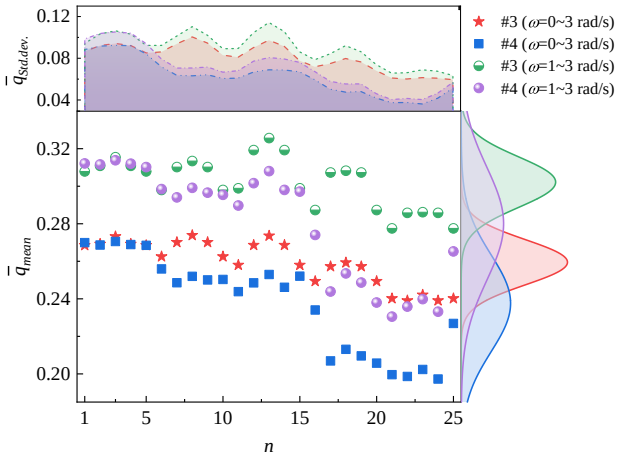

Fig. 22. Energy capture performance $\overline{q}_{mean}$ of the WEC units under the #3 and #4 configurations within the frequency ranges $\omega \in [0, 3]$ rad/s and $\omega \in [1, 3]$ rad/s, along with the corresponding marginal and variance distributions.

Figure 23 illustrates wave height distributions for #3 and #4 arrays under three submersion conditions ($z_n/R = 0$, 0.7 and 1.0), delineating contributions from incident, diffraction, and radiation potentials. Visual inspection reveals maximal wave amplification in the FB array, particularly for #4 configuration, which attains a peak wave height of 3.63 m accompanied by a well-defined trapped mode signature. As the submergence depth increases, the wave height diminishes significantly, and the wave surface becomes smoother. For example, #3 array at $z_n/R = 1$ demonstrates a maximum wave height of 1.08 m, closely approximating the incident wave amplitude ($A = 1$ m) with sub-5% deviation. Inter-array comparisons indicate that wave elevations associated with #4 array substantially exceed those

of #3 array, with the latter configuration displaying reduced wave surface perturbation. Therefore, for the CETO model at $z_n/R = 1$, compared to the #4 array, the #3 array exhibits more uniform energy capture across the WEC units, higher total captured power, and a gentler wave surface.

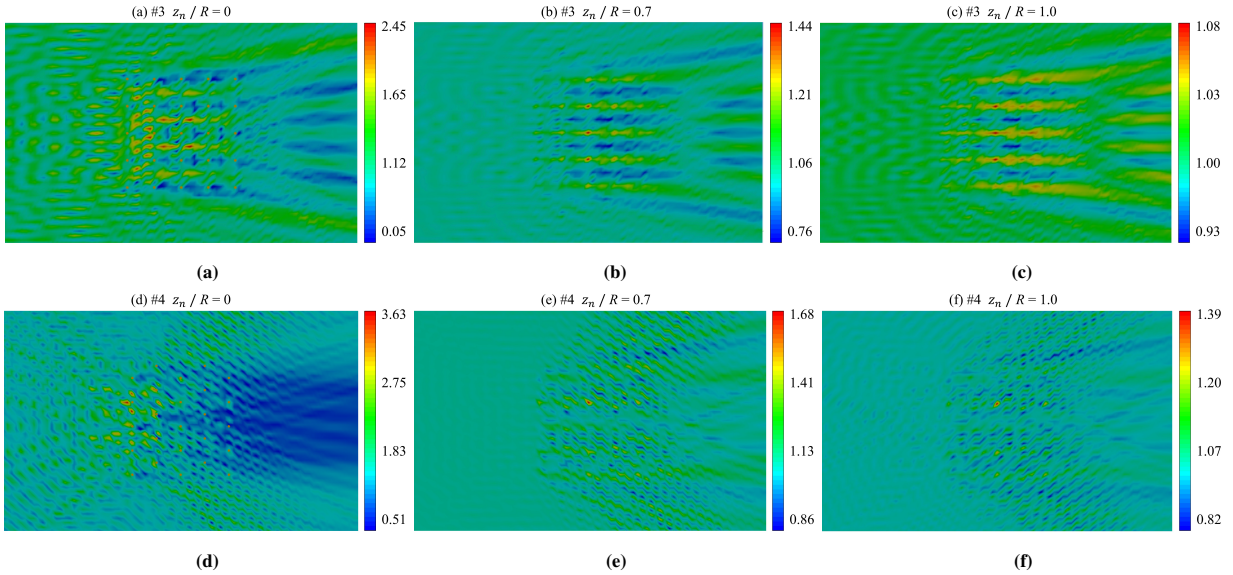

Fig. 23. The maximum free surface elevation for arrays #3 and #4 at three different submergence depths.

4.2.2. Effect of submergence

To enhance the practical relevance of this study for engineering applications, this section compares the energy capture and motion response characteristics of the FB ($z_n/R = 0$) and CETO ($z_n/R = 1$) systems for five different scales arrays (i.e., N = 4, 9, 16, 25, and 36) under the #3 configuration (see Fig. 24). This parametric study aims to identify the optimal array configuration for wave farm, specifically addressing the optimal number of WECs sub-array for deployment following the #3 configuration.

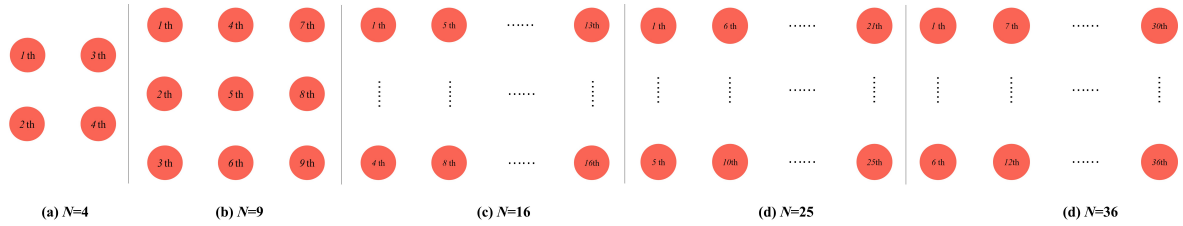

Fig. 24. Five different array scales (i.e., N = 4, 9, 16, 25, and 36 for (a) ~ (e)) under the #3 configuration.

Figures 25 and 26 delineate the energy capture characteristics of FB and CETO systems across spectral domains $\omega \in [0, 3]$ and $\omega \in [1, 3]$ rad/s, respectively, for the five different scales. In the FB systems (see Figs. 25a and 26a), pronounced shadowing effects are observed, particularly in the #4 array, where shadowing from the front row onto the back row is particularly strong. This results in a notable decline in wave energy capture efficiency with each additional row. For instance, in Fig. 25a, for $N = 4$, the average $\overline{q}_{mean}$ of the 1st and 2nd row floats are 0.37 and 0.30, respectively. For $N = 36$, sequential row averages decline as 0.38, 0.33, 0.30, 0.25, 0.18, 0.20. Marginal distribution profiles (left panels) and variance spectra (upper panels) in Figs. 25a and 26a further corroborate substantial reductions in both distribution maxima and $\overline{q}_{\text{Std.dev}}$ magnitudes with increasing N. Conversely, CETO configurations (Figs. 25b and 26b) exhibit significantly attenuated shadow effect, especially at N = 4, 9, 16. For instance, in Fig. 25a, for N = 4, 9, and 16, $\overline{q}_{mean} \in [0.25, 0.27]$; in Fig. 26b, for N = 4, 9, and 16, $\overline{q}_{mean} \in [0.20, 0.22]$. Observing the marginal distribution

curves and variance curves in Figs. 25b and 26b, it can be seen that the peak values of the marginal distribution curves and the variance curves remain relatively stable, with no significant reduction, especially for $N = 4$, 9, and 16.

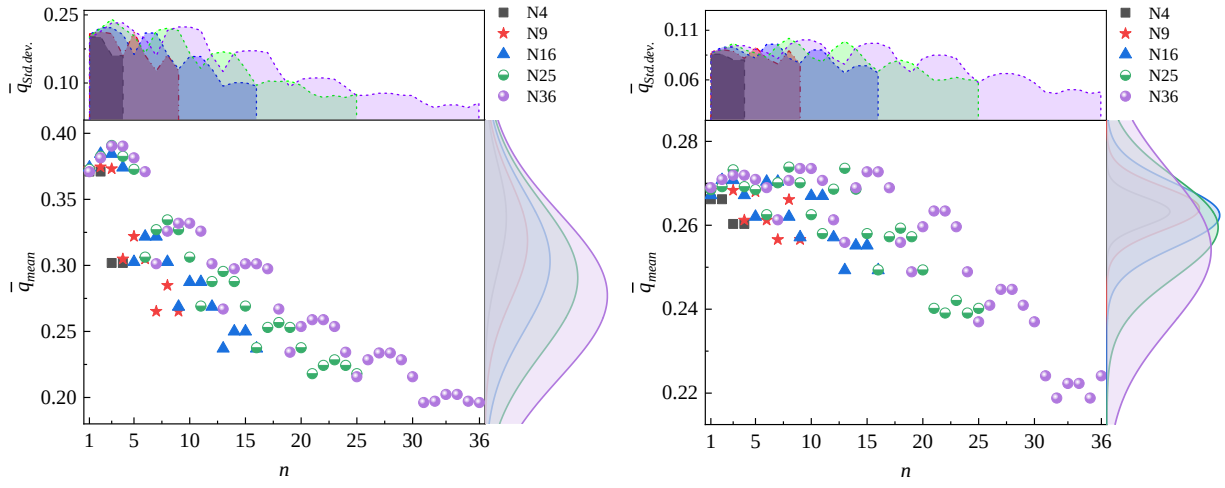

(a) FB system **(b)** CETO system

Fig. 25. Energy capture performance $\overline{q}_{mean}$ of the WEC units in the five different scale arrays across spectral domain $\omega \in [0, 3]$ rad/s under the #3 configuration, along with the corresponding marginal distributions and variance distributions.

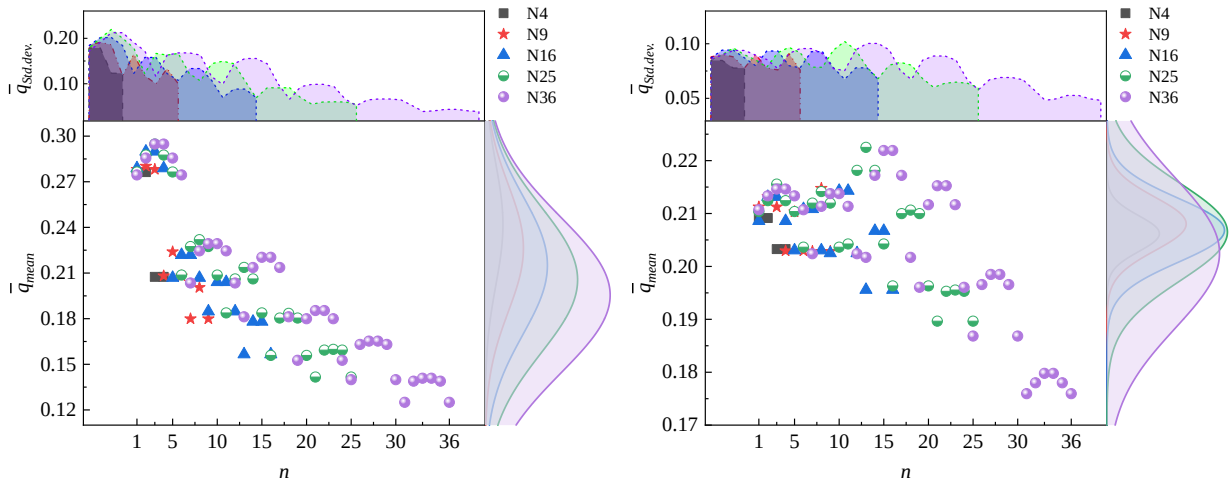

(a) FB system **(b)** CETO system

Fig. 26. Energy capture performance $\overline{q}_{mean}$ of the WEC units in the five different scale arrays across spectral domain $\omega \in [1, 3]$ rad/s under the #3 configuration, along with the corresponding marginal distributions and variance distributions.

Figure 27 comparatively analyzes FB and CETO systems across five array scales using normalized spectral metrics $\overline{A}_{\text{all}}$ and $\overline{A}_{1-3}$. The analysis reveals a monotonic increase in the ratio of integrated spectral areas between FB and CETO arrays with expanding array dimensions. Specifically, within the lower frequency regime ($\omega \in [0, 3]$ rad/s), this ratio escalates from 78% to 92% as the unit count N increases, while the higher frequency range ($\omega \in [1, 3]$ rad/s) exhibits a more pronounced enhancement from 85% to 103%. Crucially, for large-scale configurations ($N = \{16, 25, 36\}$), the systems demonstrate near-equivalent spectral coverage, with FB-to-CETO bandwidth ratios achieving 96%, 100%, and 103%, respectively.

Given that the motion response and wave energy capture for both FB and CETO systems under an incident wave

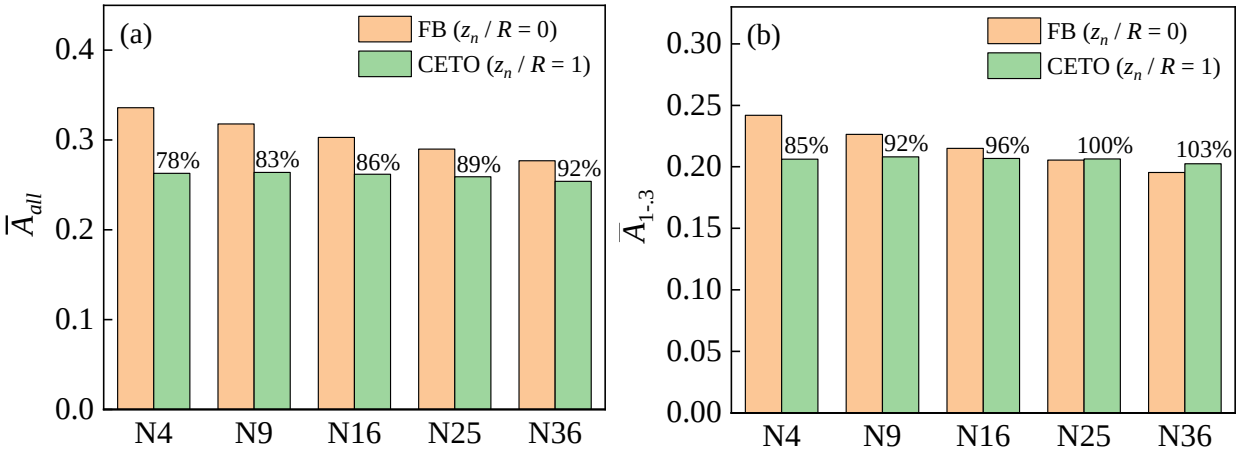

Fig. 27. Wave energy capture performance of the FB and CETO systems in five different scale arrays under the #3 configuration.

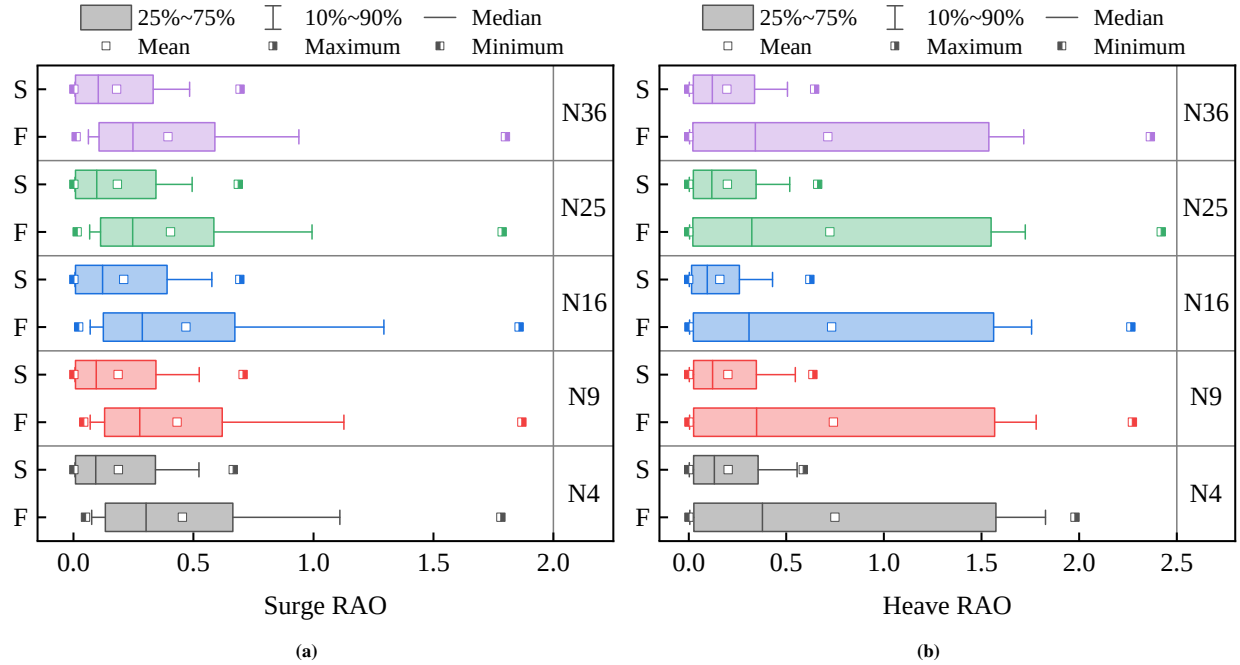

Fig. 28. Box plots of the surge and heave RAO for five arrays of varying scales in the #3 arrangement, where F represents the FB WEC (z_n/R = 0) and S represents the CETO WEC (z_n/R = 1).

angle of 0 deg are mainly concentrated in the surge and heave modes [60, 14], both motion of FB (i.e., z_n/R = 0, denoted as F) and CETO (i.e., z_n/R = 1, denoted as S) are investigated in Fig. 28. Overall, the surge and heave RAOs of the FB system are significantly larger than those of the CETO system. Specifically, in the surge mode, the maximum value of the FB system is approximately 2.5 times that of the CETO system, while the mean and median values of the FB system are 2.5 and 2.3 times greater than those of the CETO system (i.e., maximums: 1.8 vs. 0.65; means: 0.45 vs. 0.2; medians: 0.35 vs. 0.15). Furthermore, the statistical distributions presented in Fig. 28a demonstrate remarkable consistency across five array scales ($N = \{4, 9, 16, 25, 36\}$), though notable disparities emerge in the FB configuration - particularly in the maximum value in the region of 10%-90%. In the heave mode, the CETO system exhibits significantly greater stability than the FB system, For instance, the average maximum RAO of the FB system is approximately 3.75 times that of the CETO system (i.e., 2.25 vs. 0.60), and the maximum value in the region of

10% − 90% and mean values of the FB system are 4.21 and 3.75 times greater than those of the CETO system (i.e., 1.6 vs. 0.38, 0.75 vs. 0.2). Notably, FB systems achieve minimal heave RAO magnitudes at $N = 4$, whereas CETO configurations optimize operational stability at $N = 16$.

Overall, the dynamic response characteristics of the FB and CETO arrays are examined in this subsection by analyzing the #3 configuration across five different array scales, leading to the following conclusions. In terms of wave energy capture, the shadow effect in the CETO array is markedly reduced, and the captured power of each unit in the array is more evenly distributed, with weaker heterogeneity across units, particularly for N=4, 9, and 16. Although $\overline{A}_{all}$ of the FB system is greater than that of CETO in the region of $\omega \in [0, 3]$ rad/s, the area ratio of FB and CETO decreases significantly as N increases. More importantly, within the frequency range $\omega \in [1, 3]$ rad/s, when N=16, 25, and 36, the captured power of the FB and CETO arrays is nearly identical. In terms of motion response, the motion RAO of the CETO system is significantly smaller than that of the FB system, with the average motion RAO reduced by more than 2.5 times, especially in the #3 array with $N = 16$. Given the above analysis of energy capture and motion response, in engineering applications, the #3 configuration and $N = 16$ can be used as sub-arrays to construct the entire CETO WECs system.

5. Conclusions

In this study, the potential functions for each domain of the FB and CETO array-based systems are derived by applying the matching-method of eigenfunctions and the Taylor series expansion method under boundary conditions to evaluate the wave-structure interaction. In accordance with the principles of fluid continuity, a system of linear equations is established to solve for the unknown coefficients of the potential functions. After obtaining the wave excitation force, radiation added mass and damping, the energy capture and kinematic response of the FB and CETO are solved based on the coupled motion equations, incorporating the effects of PTO damping, stiffness, and mooring lines.

After completing the analytical modeling, the model validation consists of five parts: hydrodynamic convergence validation, based on the largest configuration of the array examined in this study (i.e., N=36); verification of the hydrodynamic coefficient calculation accuracy, drawing on the research of Jiang et al. [77, 78]; dynamic response validation for the FB system, based on model test; kinematic and energy capture validation for the CETO system, informed by the work of Sergiienko et al. [14, 60]; and motion response validation for the FB and CETO arrays, based on AMA-system [23]. In the validation cases, the analytical model exhibits strong alignment with existing published data and results obtained through alternative methodologies. Following model validation, the analytical model is employed to perform a multimode impact analysis of FB and CETO systems. The main findings are listed in order of significance as follows.

(i) Regarding wave energy capture for standalone FB and CETO systems, a marked distinction is observed when compared to array-based FB and CETO systems. Specifically, the standalone FB system significantly outperforms the CETO system for wave energy capture, given that the motion of water particles diminishes with increasing water depth. Under diffraction and radiation wave interactions, the array-based FB system experiences a significant shadow effect (even if the separation distance between WECs reaches 20 times the radius), resulting in substantially higher energy capture for the front-row WECs compared to the rear-row floats. This phenomenon also leads to amplified motion and energy capture for specific individual floats, potentially increasing the risk of damage. In contrast, the shadow effect is markedly diminished in the array-based CETO system, wherein energy capture is more evenly distributed across the WEC units, enhancing motion stability significantly, and energy capture performance rivals that of the FB system in certain configurations. Therefore, the comparative analysis of FB and CETO systems should be conducted in an array-based framework, with CETO arrays offering considerable potential for future engineering applications.

(ii) For the two distinct array configurations commonly utilized in engineering applications (i.e., orthogonal array #3 and staggered array #4, corresponding to Figs. 17c and 17d), the staggered array outperforms the orthogonal array in the FB system ($z_n/R = 0$), whereas the orthogonal array demonstrates enhanced effectiveness in the CETO system ($z_n/R = 0.7, 1, 1.5$). This distinction is primarily evidenced by higher total captured power, a more uniform distribution of energy captured by each unit of the array, and a gentler wave surface.

(iii) By investigating the impact of sub-array configurations on engineering layouts, it has been determined that the CETO system can be effectively deployed in sub-array modules within specific sea areas to mitigate shadow effect and enhance wave energy capture. Notably, under the orthogonal layout, the wave energy capture efficiency of the FB array diminishes as the number of floats increases in the sub-array. In contrast, for the CETO system, when the sub-array scale at $N = 4, 9, 16$, the wave energy capture efficiency remains stable, with the energy distribution among each WEC unit in the array remaining relatively uniform.

(iv) A multi-parameter investigation of the CETO system reveals that the PTO damping and stiffness significantly influence the bandwidth and peak magnitude of the wave energy capture-incident wave frequency curve, which typically exhibits a single-peak mode. In contrast to PTO damping, stiffness affects the bandwidth and peak frequency of the energy capture curve, a critical consideration for designing CETO systems tailored to specific sea conditions (e.g., aligning the energy capture bandwidth with the incident wave spectrum). Although the radius, thickness, and submergence depth of the CETO have important effects on the motion RAO and wave energy capture efficiency, where the response-frequency curve generally maintains a single-peak mode, the radius, in contrast to thickness and submergence depth, plays a pivotal role in affecting the bandwidth and peak frequency, akin to the effect of PTO stiffness. Consequently, in engineering optimization under specific sea conditions, the optimized variables can be classified (e.g., parameters modulating bandwidth and peak frequency versus those that remain unaffected), enabling local optimization to be performed prior to global multi-parameter optimization. This approach improves optimization efficiency while ensuring robustness.

Finally, grounded in the developed analytical modeling framework, the present study effectively captures the essential hydrodynamic interactions within floating and submerged WEC arrays, providing reliable first-order predictions of array performance. From an engineering perspective, the proposed approach proves particularly valuable during the conceptual design and parametric optimization stages, where it enables rapid evaluation of array layouts, identification of shadowing and resonance tendencies, and efficient pre-screening of configurations prior to detailed CFD simulations or experimental tests. Furthermore, this framework bridges the gap between theoretical hydrodynamics and engineering implementation, offering a computationally efficient and physically transparent tool for early-stage design and performance assessment of wave energy systems. It should be noted that the LCoE, engineering feasibility, and the effects of extreme sea conditions on the device are not addressed in this study. Nonetheless, from the perspectives of energy capture and motion response performances, it can be inferred that array-based submerged WECs may have significant potential for future development.

Declaration of competing interest

The authors declare that they have no known competing financial interests or personal relationships that could have appeared to influence the work reported in this paper.

Data Availability Statement

Data will be made available on request.

Acknowledgements

The authors would like to acknowledge the support of the National Natural Science Foundation of China (Grant No. 52271297), Shandong Provincial Natural Science Foundation (Grant No. ZR2021ZD23), Shandong Provincial Natural Science Foundation (Grant No. ZR2022ME002), National Natural Science Foundation of China (Grant No. U22A20216).

Nomenclature

A	Amplitude of incident wave
$A(\omega)$	The matrix of radiation added mass at ω
$\overline{A}_{all}$	The frequency band area over the frequency range of 0 to 3 rad/s, i.e., $\overline{A}_{all} = \frac{\sum_{i=1}^{N} \int_0^3 q_n(\omega) d\omega}{N}$
$\overline{A}_{1-3}$	The frequency band area over the frequency range of 1 to 3 rad/s, i.e., $\overline{A}_{1-3} = \frac{\sum_{i=1}^{N} \int_1^3 q_n(\omega) d\omega}{N}$
$a_{p,i}^{n,j}$	Radiation added mass of float n in jth mode due to the oscillating of float p in ith mode
α_h	The angle between adjacent mooring lines in the horizontal plane
α_v	The angle between adjacent mooring lines in the vertical plane
$B(\omega)$	The matrix of radiation damping at ω
B_{pto}	The damping matrix due to the PTO system and mooring lines
$\overline{B}_{pto}$	The non-dimensionalized of PTO damping
$b_{p,i}^{n,j}$	Radiation damping in jth mode due to the oscillating of float p in ith mode
$\boldsymbol{C}_s$	The hydrostatic restoring matrix
C_{pto}	Counteracting hydrostatic pressure forces at undisturbed locations, i.e., $C_{pto} = -((\rho V - M_m))/(3\cos\alpha_v)$
d	Total draft of WEC
$d_s^{(n)}$	The submersion depth of the upper surface of the float n
$d_t^{(n)}$	The thickness of the float n
$d_1^{(n)}, d_2^{(n)}$	For FB system, $d_1^{(n)}$ is draft depth, and for CETO system, $d_1^{(n)} = d_s^{(n)}$, $d_2^{(n)} = d_s^{(n)} + d_t^{(n)}$
$F_{\chi}^{n,i'}$	The force on cylinder n in mode i'
g	Gravitational acceleration
h	Water depth
J	Vertical cut-offs number ($j = 0, 1, 2, ..., J$)
k_0	Incident wave number
$k_{q,0}^{(n)}$	Wave number for propagating mode in the region Ω_q^n
$k_{q,j}^{(n)}$	Wave number for evanescent modes in the region Ω_q^n ($j \geq 1$)
K_{pto}	The stiffness matrix due to the PTO system and mooring lines
$\overline{K}_{pto}$	The non-dimensionalized of PTO stiffness
l_0	The initial tether length
M	Angular cut-offs number ($m = -M, ..., 0, ..., M$)
$\boldsymbol{M}_m$	The structure mass matrix

N	Total number of floats
$\overline{P}_w$	The time-averaged power output by WECs array
P_{max}	The maximum absorbed power by an axisymmetric body in monochromatic waves
q	Factor for evaluating the wave energy capture efficiency of WECs, i.e., $q = P_w/P_{max}$
$\overline{q}_n$	The average q factor for each WEC over the frequency range of 0 to 3 rad/s
$\overline{q}_{array}$	The average $q_n(\omega)$ of all WECs in the array at a given frequency ω, i.e., $\overline{q}_{array} = \frac{\sum_{n=1}^{N} q_n(\omega)}{N}$, where $q_n(\omega)$ is the q factor of the nth WEC at ω)
$\overline{q}_{mean}$	Mean value of $\overline{q}_n$ for all WECs in the array, i.e., $\overline{q}_{mean} = \frac{\sum_{i=1}^{N} \overline{q}_n}{N}$
$q_{Std.dev}$	The variance corresponding to the $\overline{q}_n$ of all WECs in the array, i.e., $q_{Std.dev} = \frac{\sum_{i=1}^{N} [\overline{q}_n - \overline{q}_{mean}]^2}{N}$
$R^{(n)}$	The radius of the float n
S_m	System stiffness
$\boldsymbol{X}$	The complex amplitude column vector of displacement vectors for N structures
$\dot{\boldsymbol{X}}$	The complex velocity column vector
$\overline{X}_{i,max}$	The maximum motion response amplitude of all WECs in the ith mode
β	Wave incident angle
ϕ	The total spatial velocity potential
ϕ_S	The scattering spatial velocity potential
ϕ_I	Incident wave potential
ϕ_D	Diffraction spatial velocity potential
$\phi_{p,i}$	Radiation spatial velocity potential due to unit amplitude velocity oscillation of float p oscillating in the ith mode
δ	The Kronecker delta
ρ	Mass Density of water
ω	Incident wave angular frequency
ω_0	Bandwidth of dynamic response
ω_r	Peak frequency
(x,y,z)	Cartesian coordinate system
(r, θ, z)	Cylindrical coordinate system
$(0, \theta, z_n)$	Centre of rotation of the float n

References

[1] D. P. Rijnsdorp, J. E. Hansen, R. J. Lowe, Simulating the wave-induced response of a submerged wave-energy converter using a non-hydrostatic wave-flow model, Coastal Engineering 140 (2018) 189–204. URL: https://www.sciencedirect.com/science/article/pii/S0378383917306440. doi:https://doi.org/10.1016/j.coastaleng.2018.07.004.

[2] H. Shi, F. Cao, Z. Liu, N. Qu, Theoretical study on the power take-off estimation of heaving buoy wave energy converter, Renewable Energy 86 (2016) 441–448. URL: https://www.sciencedirect.com/science/article/pii/S0960148115302275. doi:https://doi.org/10.1016/j.renene.2015.08.027.

[3] A. jun Li, Y. Liu, X. Liu, Y. Zhao, Analytical and experimental studies on water wave interaction with a submerged perforated quarter-circular caisson breakwater, Applied Ocean Research 101 (2020) 102267. URL: https://www.sciencedirect.com/science/article/pii/S0141118720301449. doi:https://doi.org/10.1016/j.apor.2020.102267.

[4] C. Zhao, P. R. Thies, L. Johanning, Investigating the winch performance in an asv/rov autonomous inspection system, Applied Ocean Research 115 (2021) 102827. URL: https://www.sciencedirect.com/science/article/pii/S0141118721002996. doi:https://doi.org/10.1016/j.apor.2021.102827.

[5] C. W. E. Limited, Carnegie clean energy, 2024. URL: https://www.carnegiece.com, accessed: 2024-12-09.

[6] D. R. David, A. Kurniawan, H. Wolgamot, J. E. Hansen, D. Rijnsdorp, R. Lowe, Nearshore submerged wave farm optimisation: A multi-objective approach, Applied Ocean Research 124 (2022) 103225. URL: https://www.sciencedirect.com/science/article/pii/S014111872200164X. doi:https://doi.org/10.1016/j.apor.2022.103225.

[7] S. Astariz, G. Iglesias, Selecting optimum locations for co-located wave and wind energy farms. part ii: A case study, Energy Conversion and Management 122 (2016) 599–608. URL: https://www.sciencedirect.com/science/article/pii/S0196890416304630. doi:https://doi.org/10.1016/j.enconman.2016.05.078.

[8] K. Zhu, H. Shi, J. Tao, H. Gong, Z. Han, F. Cao, Analytical study on hydrodynamic performance of co-located offshore wind–solar farms, Physics of Fluids 36 (2024) 013325. URL: https://doi.org/10.1063/5.0187178. doi:10.1063/5.0187178.

[9] M. Callan, C. M. Linton, D. V. Evans, Trapped modes in two-dimensional waveguides, Journal of Fluid Mechanics 229 (1991) 51–64. doi:10.1017/S0022112091002938.

[10] R. Porter, D. V. Evans, The trapping of surface waves by multiple submerged horizontal cylinders, Journal of Engineering Mathematics 34 (1998) 417–433. URL: https://doi.org/10.1023/A:1004361929350. doi:10.1023/A:1004361929350.

[11] Y. LI, C. C. MEI, Bragg scattering by a line array of small cylinders in a waveguide. part 1. linear aspects, Journal of Fluid Mechanics 583 (2007) 161–187. doi:10.1017/S0022112007006131.

[12] N. Tran, N. Sergiienko, B. Cazzolato, M. Ghayesh, M. Arjomandi, Design considerations for a three-tethered point absorber wave energy converter with nonlinear coupling between hydrodynamic modes, Ocean Engineering 254 (2022) 111351. URL: https://www.sciencedirect.com/science/article/pii/S0029801822007399. doi:https://doi.org/10.1016/j.oceaneng.2022.111351.

[13] M. H. Jahangir, S. Ghanbari Motlagh, Feasibility study of ceto wave energy converter in iranian coastal areas to meet electrical demands (a case study), Energy for Sustainable Development 70 (2022) 272–289. URL: https://www.sciencedirect.com/science/article/pii/S0973082622001247. doi:https://doi.org/10.1016/j.esd.2022.07.017.

[14] N. Sergiienko, B. Cazzolato, B. Ding, P. Hardy, M. Arjomandi, Performance comparison of the floating and fully submerged quasi-point absorber wave energy converters, Renewable Energy 108 (2017) 425–437. URL: https://www.sciencedirect.com/science/article/pii/S0960148117301829. doi:https://doi.org/10.1016/j.renene.2017.03.002.

[15] Stratigaki, Vicky and Troch, Peter and Forehand, David and Stallard, et al., Physical modelling of large wave energy converter arrays in a large-scale wave basin: the WECwakes project, in: Hydralab IV Closing Conference, Proceedings, 2014, pp. 1–11.

[16] V. Stratigaki, P. Troch, T. Stallard, D. Forehand, J. P. Kofoed, M. Folley, M. Benoit, A. Babarit, J. Kirkegaard, Wave basin experiments with large wave energy converter arrays to study interactions between the converters and effects on other users in the sea and the coastal area, Energies 7 (2014) 701–734. URL: https://www.mdpi.com/1996-1073/7/2/701. doi:10.3390/en7020701.

[17] P. Stansby, S. Draycott, M4 wec development and wave basin froude testing, European Journal of Mechanics - B/Fluids 104 (2024) 182–193. URL: https://www.sciencedirect.com/science/article/pii/S0997754623001802. doi:https://doi.org/10.1016/j.euromechflu.2023.12.007.

[18] T. Vervaet, V. Stratigaki, B. De Backer, K. Stockman, M. Vantorre, P. Troch, Experimental modelling of point-absorber wave energy converter arrays: A comprehensive review, identification of research gaps and design of the wecfarm setup, Journal of Marine Science and Engineering 10 (2022). URL: https://www.mdpi.com/2077-1312/10/8/1062. doi:10.3390/jmse10081062.

[19] F. Cao, M. Yu, M. Han, B. Liu, Z. Wei, J. Jiang, H. Tian, H. Shi, Y. Li, Wecs microarray effect on the coupled dynamic response and power performance of a floating combined wind and wave energy system, Renewable Energy 219 (2023) 119476. URL: https://www.sciencedirect.com/science/article/pii/S0960148123013915. doi:https://doi.org/10.1016/j.renene.2023.119476.

[20] B. Zhou, Y. Wang, Z. Zheng, P. Jin, D. Ning, Power generation and wave attenuation of a hybrid system involving a heaving cylindrical wave energy converter in front of a parabolic breakwater, Energy 282 (2023) 128364. URL: https://www.sciencedirect.com/science/article/pii/S0360544223017589. doi:https://doi.org/10.1016/j.energy.2023.128364.

[21] M. Göteman, J. Engström, M. Eriksson, J. Isberg, Optimizing wave energy parks with over 1000 interacting point-absorbers using an approximate analytical method, International Journal of Marine Energy 10 (2015) 113–126. URL: https://www.sciencedirect.com/science/article/pii/S2214166915000119. doi:https://doi.org/10.1016/j.ijome.2015.02.001.

[22] S. Zhan, P. Stansby, Z. Liao, G. Li, A fast model predictive control framework for multi-float and multi-mode-motion wave energy converters, IEEE Transactions on Control Systems Technology 31 (2023) 1443–1450. doi:10.1109/TCST.2022.3216081.

[23] K. Zhu, H. Shi, M. Han, F. Cao, Layout study of wave energy converter arrays by an artificial neural network and adaptive genetic algorithm, Ocean Engineering 260 (2022) 112072. URL: https://www.sciencedirect.com/science/article/pii/S0029801822014007. doi:https://doi.org/10.1016/j.oceaneng.2022.112072.

[24] M. Han, H. Shi, F. Cao, K. Zhu, B. Liu, M. Yu, Z. Wei, Dynamic characteristics and parameter analysis of a floating hybrid wind-wave energy

system based on a novel coupled numerical framework, Energy Conversion and Management 312 (2024) 118558. URL: https://www.sciencedirect.com/science/article/pii/S0196890424004990. doi:https://doi.org/10.1016/j.enconman.2024.118558.
[25] H. Zhang, J. Zhao, S. Xu, T. Wang, M. Elsakka, C. Guedes Soares, Hydrodynamic characteristics of a novel towerless floating wind turbine integrated with wave energy converters, Physics of Fluids 37 (2025) 057108. URL: https://doi.org/10.1063/5.0267231. doi:10.1063/5.0267231.
[26] M. Giassi, J. Engström, J. Isberg, M. Göteman, Comparison of wave energy park layouts by experimental and numerical methods, Journal of Marine Science and Engineering 8 (2020). URL: https://www.mdpi.com/2077-1312/8/10/750. doi:10.3390/jmse8100750.
[27] H. Zhang, T. Wang, L. Chen, H. Shi, C. Guedes Soares, Numerical study on wave run-up and forces on a fixed cylinder under linear and nonlinear focused waves, Ocean Engineering 300 (2024) 117456. URL: https://www.sciencedirect.com/science/article/pii/S0029801824007935. doi:https://doi.org/10.1016/j.oceaneng.2024.117456.
[28] F. Cao, M. Han, H. Shi, M. Li, Z. Liu, Comparative study on metaheuristic algorithms for optimising wave energy converters, Ocean Engineering 247 (2022) 110461. URL: https://www.sciencedirect.com/science/article/pii/S002980182101742X. doi:https://doi.org/10.1016/j.oceaneng.2021.110461.
[29] S. Zheng, R. Porter, D. Greaves, Wave scattering by an array of metamaterial cylinders, Journal of Fluid Mechanics 903 (2020) A50. doi:10.1017/jfm.2020.660.
[30] A. ANSYS, ANSYS Aqwa User's Manual, ANSYS Inc, United States, 2025. URL: https://ansyshelp.ansys.com/public/Views/Secured/corp/v251/en/pdf/Aqwa_Users_Manual.pdf.
[31] I. WAMIT, WAMIT USER MANUAL, MIT, United States, 1998. URL: https://www.wamit.com/. doi:https://doi.org/10.1142/9789813147195_0001.
[32] J. M. Jonkman, M. L. Buhl, Jr, FAST User's Guide - Updated August 2005, Technical Report NREL/TP-500-38230, National Renewable Energy Lab.(NREL), 2005. URL: https://www.osti.gov/biblio/15020796. doi:10.2172/15020796.
[33] H. Team, Hydrostar guide: Hydrodynamic calculation software, Software, 2024. URL: https://marine-offshore.bureauveritas.com/hydrostar-software-powerful-hydrodynamic.
[34] T. S. team, SWAN USER MANUAL, 2024. URL: https://swanmodel.sourceforge.io/download/zip/swanuse.pdf.
[35] S. Astariz, C. Perez-Collazo, J. Abanades, G. Iglesias, Towards the optimal design of a co-located wind-wave farm, Energy 84 (2015) 15–24. URL: https://www.sciencedirect.com/science/article/pii/S0360544215002509. doi:https://doi.org/10.1016/j.energy.2015.01.114.
[36] S. Zheng, H. Liang, D. Greaves, Wave scattering and radiation by a surface-piercing vertical truncated metamaterial cylinder, Journal of Fluid Mechanics 983 (2024) A7. doi:10.1017/jfm.2024.147.
[37] H. Kagemoto, D. K. P. Yue, Interactions among multiple three-dimensional bodies in water waves: an exact algebraic method, Journal of Fluid Mechanics 166 (1986) 189–209. doi:10.1017/S0022112086000101.
[38] A. Williams, A. Abul-Azm, Hydrodynamic interactions in floating cylinder arrays—ii. wave radiation, Ocean Engineering 16 (1989) 217–263. URL: https://www.sciencedirect.com/science/article/pii/002980188990019X. doi:https://doi.org/10.1016/0029-8018(89)90019-X.
[39] P. Siddorn, R. Eatock Taylor, Diffraction and independent radiation by an array of floating cylinders, Ocean Engineering 35 (2008) 1289–1303. URL: https://www.sciencedirect.com/science/article/pii/S0029801808001285. doi:https://doi.org/10.1016/j.oceaneng.2008.06.003.
[40] X. Zeng, Q. Wang, M. Shi, Y. Kang, F. Yu, Hydrodynamic interactions between waves and cylinder arrays of relative motions composed of truncated floating cylinders with five degrees of freedom, Journal of Fluids and Structures 115 (2022) 103785. URL: https://www.sciencedirect.com/science/article/pii/S0889974622001773. doi:https://doi.org/10.1016/j.jfluidstructs.2022.103785.
[41] X. Zeng, Y. Kang, G. Wang, Z. Xue, F. Yu, Approximate calculation method of hydrodynamic solution of an array with a large number of truncated cylinders, Ocean Engineering 257 (2022) 111693. URL: https://www.sciencedirect.com/science/article/pii/S0029801822010484. doi:https://doi.org/10.1016/j.oceaneng.2022.111693.
[42] B. Child, V. Venugopal, Optimal configurations of wave energy device arrays, Ocean Engineering 37 (2010) 1402–1417. URL: https://www.sciencedirect.com/science/article/pii/S0029801810001447. doi:https://doi.org/10.1016/j.oceaneng.2010.06.010.
[43] R. W. Yeung, Added mass and damping of a vertical cylinder in finite-depth waters, Applied Ocean Research 3 (1981) 119–133. URL: https://www.sciencedirect.com/science/article/pii/0141118781901012. doi:https://doi.org/10.1016/0141-1187(81)90101-2.
[44] X. Zeng, Q. Wang, Y. Kang, F. Yu, Hydrodynamic interactions among wave energy converter array and a hierarchical genetic algorithm for layout optimization, Ocean Engineering 256 (2022) 111521. URL: https://www.sciencedirect.com/science/article/pii/S0029801822008903. doi:https://doi.org/10.1016/j.oceaneng.2022.111521.
[45] S. Zheng, Y. Zhang, G. Iglesias, Wave–structure interaction in hybrid wave farms, Journal of Fluids and Structures 83 (2018) 386–412. URL: https://www.sciencedirect.com/science/article/pii/S0889974618302937. doi:https://doi.org/10.1016/j.jfluidstructs.2018.09.012.
[46] S. Zheng, Y. Zhang, Theoretical modelling of a new hybrid wave energy converter in regular waves, Renewable Energy 128 (2018) 125–141. URL: https://www.sciencedirect.com/science/article/pii/S096014811830572X. doi:https://doi.org/10.1016/j.renene.2018.05.051.
[47] L. Cui, S. Zheng, Y. Zhang, J. Miles, G. Iglesias, Wave power extraction from a hybrid oscillating water column-oscillating buoy wave energy converter, Renewable and Sustainable Energy Reviews 135 (2021) 110234. URL: https://www.sciencedirect.com/science/article/pii/S1364032120305232. doi:https://doi.org/10.1016/j.rser.2020.110234.
[48] K. Zhu, H. Shi, S. Zheng, S. Michele, F. Cao, Hydrodynamic analysis of hybrid system with wind turbine and wave energy converter, Applied Energy 350 (2023) 121745. URL: https://www.sciencedirect.com/science/article/pii/S0306261923011091. doi:https://doi.org/10.1016/j.apenergy.2023.121745.

[49] K. Zhu, S. Zheng, S. Michele, F. Cao, H. Shi, Theoretical modeling of a co-located system with a floating wind platform and vertical truncated cylinders array, Renewable Energy 223 (2024) 120025. URL: https://www.sciencedirect.com/science/article/pii/S0960148124000909. doi:https://doi.org/10.1016/j.renene.2024.120025.
[50] E. Renzi, S. Michele, S. Zheng, S. Jin, D. Greaves, Niche applications and flexible devices for wave energy conversion: A review, Energies 14 (2021). URL: https://www.mdpi.com/1996-1073/14/20/6537.
[51] S. Michele, F. Buriani, E. Renzi, Power extraction from floating elastic plates, International Marine Energy Journal 5 (2022) 209–218. URL: https://marineenergyjournal.org/imej/article/view/124. doi:10.36688/imej.5.209-218.
[52] S. Michele, S. Zheng, D. Greaves, Wave energy extraction from a floating flexible circular plate, Ocean Engineering 245 (2022) 110275. URL: https://www.sciencedirect.com/science/article/pii/S002980182101581X. doi:https://doi.org/10.1016/j.oceaneng.2021.110275.
[53] A.-J. Li, H. Fang, Y. Liu, Hydroelastic analysis of interaction between water waves and a floating laminated disk, Physics of Fluids 34 (2022) 047121. URL: https://aip.scitation.org/doi/10.1063/5.0088675. doi:https://doi.org/10.1063/5.0088675.
[54] S. Zheng, S. Michele, H. Liang, M. H. Meylan, D. Greaves, Wave power extraction from a floating elastic disk-shaped wave energy converter, Journal of Fluid Mechanics 948 (2022) A38. doi:https://doi.org/10.1017/jfm.2022.701.
[55] S. Zheng, M. H. Meylan, G. Zhu, D. Greaves, G. Iglesias, Hydroelastic interaction between water waves and an array of circular floating porous elastic plates, Journal of Fluid Mechanics 900 (2020) A20. doi:https://doi.org/10.1017/jfm.2020.508.
[56] S. Michele, E. Renzi, A. Borthwick, C. Whittaker, A. Raby, Weakly nonlinear theory for dispersive waves generated by moving seabed deformation, Journal of Fluid Mechanics 937 (2022) A8. doi:10.1017/jfm.2022.94.
[57] S. Michele, E. Renzi, P. Sammarco, Weakly nonlinear theory for a gate-type curved array in waves, Journal of Fluid Mechanics 869 (2019) 238–263. doi:10.1017/jfm.2019.223.
[58] B. Li, A mathematical model for weakly nonlinear water wave propagation, Wave Motion 47 (2010) 265–278. URL: https://www.sciencedirect.com/science/article/pii/S0165212509001206. doi:https://doi.org/10.1016/j.wavemoti.2009.12.003.
[59] X. Wang, P. L.-F. Liu, An explicit finite difference model for simulating weakly nonlinear and weakly dispersive waves over slowly varying water depth, Coastal Engineering 58 (2011) 173–183. URL: https://www.sciencedirect.com/science/article/pii/S0378383910001407. doi:https://doi.org/10.1016/j.coastaleng.2010.09.008.
[60] N. Sergiienko, A. Rafiee, B. Cazzolato, B. Ding, M. Arjomandi, Feasibility study of the three-tether axisymmetric wave energy converter, Ocean Engineering 150 (2018) 221–233. URL: https://www.sciencedirect.com/science/article/pii/S002980181730793X. doi:https://doi.org/10.1016/j.oceaneng.2017.12.055.
[61] X. hui ZENG, S. yi TANG, The hydrodynamic interactions of an array of truncated circular cylinders as each cylinder oscillates independently with different prescribed modes, Journal of Hydrodynamics, Ser. B 25 (2013) 27–38. URL: https://www.sciencedirect.com/science/article/pii/S1001605813603352. doi:https://doi.org/10.1016/S1001-6058(13)60335-2.
[62] D. V. Evans, A theory for wave-power absorption by oscillating bodies, Journal of Fluid Mechanics 77 (1976) 1–25. URL: https://www.cambridge.org/core/journals/journal-of-fluid-mechanics/article/abs/theory-for-wavepower-absorption-by-oscillating-bodies/CDACF97ABE7FCFB5F86FCED6019A8FC6. doi:https://doi.org/10.1017/S0022112076001109.
[63] C. C. Mei, M. A. Stiassnie, D. K.-P. Yue, Theory and Applications of Ocean Surface Waves: Part 1: Linear Aspects, World Scientific, 2005. URL: https://www.worldscientific.com/doi/abs/10.1142/9789813147195_0001?cookieSet=1. doi:https://doi.org/10.1142/9789813147195_0001.
[64] C. M. Linton, D. V. Evans, The interaction of waves with a row of circular cylinders, Journal of Fluid Mechanics 251 (1993) 687–708. doi:10.1017/S002211209300357X.
[65] I. S. Gradshteyn, I. M. Ryzhik, Table of integrals, series, and products, Academic, 1965. URL: https://www.sciencedirect.com/book/9780123849335/table-of-integrals-series-and-products.
[66] B. Z. Zhou, G. X. Wu, Resonance of a tension leg platform exited by third-harmonic force in nonlinear regular waves, Philosophical Transactions of the Royal Society A: Mathematical, Physical and Engineering Sciences 373 (2015) 20140105. URL: https://royalsocietypublishing.org/doi/abs/10.1098/rsta.2014.0105. doi:10.1098/rsta.2014.0105.
[67] B. Zhou, G. Wu, Q. Meng, Interactions of fully nonlinear solitary wave with a freely floating vertical cylinder, Engineering Analysis with Boundary Elements 69 (2016) 119–131. URL: https://www.sciencedirect.com/science/article/pii/S095579971630087X. doi:https://doi.org/10.1016/j.enganabound.2016.05.004.
[68] S. Michele, P. Sammarco, M. d'Errico, Weakly nonlinear theory for oscillating wave surge converters in a channel, Journal of Fluid Mechanics 834 (2018) 55–91. doi:10.1017/jfm.2017.724.
[69] H. Lee, S. K. Poguluri, Y. H. Bae, Performance analysis of multiple wave energy converters placed on a floating platform in the frequency domain, Energies 11 (2018). URL: https://www.mdpi.com/1996-1073/11/2/406. doi:10.3390/en11020406.
[70] S. Michele, E. Renzi, C. Perez-Collazo, D. Greaves, G. Iglesias, Power extraction in regular and random waves from an owc in hybrid wind-wave energy systems, Ocean Engineering 191 (2019) 106519. URL: https://www.sciencedirect.com/science/article/pii/S0029801819306572. doi:https://doi.org/10.1016/j.oceaneng.2019.106519.
[71] J. Hu, B. Zhou, C. Vogel, P. Liu, R. Willden, K. Sun, J. Zang, J. Geng, P. Jin, L. Cui, B. Jiang, M. Collu, Optimal design and performance analysis of a hybrid system combing a floating wind platform and wave energy converters, Applied Energy 269 (2020) 114998. URL: https://www.sciencedirect.com/science/article/pii/S0306261920305109. doi:https://doi.org/10.1016/j.apenergy.2020.114998.
[72] J. Falnes, Ocean Waves and Oscillating Systems: Linear Interactions Including Wave-Energy Extraction, Cambridge University Press, 2002. URL: https://www.cambridge.org/0521782112. doi:10.1017/CBO9780511754630.
[73] S. Zheng, A. Antonini, Y. Zhang, D. Greaves, J. Miles, G. Iglesias, Wave power extraction from multiple oscillating water columns along a straight coast, Journal of Fluid Mechanics 878 (2019) 445–480. doi:10.1017/jfm.2019.656.
[74] M. Han, F. Cao, H. Shi, H. Kou, H. Gong, C. Wang, Parametrical study on an array of point absorber wave energy converters, Ocean Engineering 272 (2023) 113857. URL: https://www.sciencedirect.com/science/article/pii/S002980182300241X. doi:https:

//doi.org/10.1016/j.oceaneng.2023.113857.
[75] K. Zhu, S. Zheng, S. Michele, F. Cao, H. Shi, D. Greaves, Wave diffraction and radiation from a semi-submersible floating foundation for wind turbines: A semi-analytical study, Physics of Fluids 35 (2023) 057120. URL: https://doi.org/10.1063/5.0149411. doi:10.1063/5.0149411.
[76] K. Zhu, H. Shi, S. Michele, M. Han, F. Cao, Analytical study on dynamic performance of a hybrid system in real sea states, Energy 290 (2024) 130259. URL: https://www.sciencedirect.com/science/article/pii/S0360544224000306. doi:https://doi.org/10.1016/j.energy.2024.130259.
[77] S. chao Jiang, Y. Gou, B. Teng, Water wave radiation problem by a submerged cylinder, Journal of Engineering Mechanics 140 (2014) 06014003. URL: https://ascelibrary.org/doi/abs/10.1061/%28ASCE%29EM.1943-7889.0000723. doi:10.1061/(ASCE)EM.1943-7889.0000723.
[78] S. chao Jiang, Y. Gou, B. Teng, D. zhi Ning, Analytical solution of a wave diffraction problem on a submerged cylinder, Journal of Engineering Mechanics 140 (2014) 225–232. URL: https://ascelibrary.org/doi/abs/10.1061/%28ASCE%29EM.1943-7889.0000637. doi:10.1061/(ASCE)EM.1943-7889.0000637.
[79] H. Zhang, T. Wang, C. Xu, H. Shi, C. Guedes Soares, Analysis on the split absorber integrated with taut-moored floating turbine, Physics of Fluids 35 (2023) 087110. URL: https://doi.org/10.1063/5.0157536. doi:10.1063/5.0157536.
[80] H. Zhang, M. Elsakka, B. Liu, S. Xu, H. Shi, Dynamic response characteristics of the taut mooring system for integrated renewable energy devices, Energy 322 (2025) 135729. URL: https://www.sciencedirect.com/science/article/pii/S0360544225013714. doi:https://doi.org/10.1016/j.energy.2025.135729.
[81] M. Han, F. Cao, H. Shi, K. Zhu, X. Dong, D. Li, Layout optimisation of the two-body heaving wave energy converter array, Renewable Energy 205 (2023) 410–431. URL: https://www.sciencedirect.com/science/article/pii/S096014812300109X. doi:https://doi.org/10.1016/j.renene.2023.01.100.